

# Neoarchean high-pressure margarite–phengitic muscovite–chlorite corona mantled corundum in quartz-free high-Mg, Al phlogopite–chlorite schists from the Bundelkhand craton, north central India

L. Saha · N. C. Pant · J. K. Pati · D. Upadhyay ·  
J. Berndt · A. Bhattacharya · M. Satynarayanan

Received: 10 October 2009 / Accepted: 15 June 2010 / Published online: 8 July 2010  
© Springer-Verlag 2010

**Abstract** In quartz-free Fe, Na-poor and high-Mg, Al schists from the Bundelkhand craton in north central India, corundum porphyroblasts in finely interleaved phlogopite–chlorite aggregates with rare clinozoisite are mantled by fine-grained (<3 µm) intergrowths of outer collars (>200 µm wide) of phengitic-muscovite and chlorite (phlogopite + corundum + H<sub>2</sub>O → phengitic-muscovite + chlorite), and <100 µm wide inner collars of margarite–

muscovite (corundum + clinozoisite + phengitic muscovite → margarite + muscovite + H<sub>2</sub>O). Wide-beam electron probe microanalyses indicate Mg in the bi-layered corona increases from corundum outwards, with a complementary decrease in Al and K. Si and Ca increase and then decrease to matrix values. The sharp chemical gradients across the highly structured bi-layered corona are inferred to suggest that the corona-forming reactions were promoted by local grain-boundary-controlled thermodynamic instability as opposed to element transport by advective diffusion. The P–T convergence of KMASH reactions and NCKMASH pseudosection phase relations computed using micro-domain compositions indicate the chlorite–phengitic muscovite outer collar formed at 18–20 kbar and ca. 630°C. The NCKMASH margarite–muscovite inner collar yielded lower metamorphic P–T conditions of 11 ± 3 kbar, ca. 630°C. U–Th–Pb chemical dating of metamorphic monazite and LA-ICPMS U–Pb isotope dating of re-equilibrated zircon yield ca. 2.78 Ga ages, which are interpreted to date corona formation and Neoarchean high-P metamorphism in the Bundelkhand craton, hitherto unknown in the Indian Precambrian. (220)

Communicated by T. L. Grove.

**Electronic supplementary material** The online version of this article (doi:[10.1007/s00410-010-0546-7](https://doi.org/10.1007/s00410-010-0546-7)) contains supplementary material, which is available to authorized users.

L. Saha  
School of Geological Sciences, University of Kwazulu-Natal,  
Private Bag X54001, Durban, South Africa

N. C. Pant  
Department of Geology, Delhi University,  
New Delhi 110 007, India

J. K. Pati  
Department of Earth and Planetary Sciences,  
Allahabad University, Allahabad 211 002, India

D. Upadhyay (✉) · A. Bhattacharya  
Department of Geology and Geophysics, Indian Institute  
of Technology, Kharagpur 721 302, India  
e-mail: dewashish@gg.iitkgp.ernet.in

D. Upadhyay · J. Berndt  
Zentrale Labor für Geochronologie, Institut für Mineralogie,  
Universität Münster, Corrensstrasse 24, 48149 Münster,  
Germany

M. Satynarayanan  
National Geophysical Research Institute, Uppal Road,  
Hyderabad 500 007, India

**Keywords** K–Mg–Al schists · Corundum · Corona texture · Archean · Bundelkhand (India) · High-pressure metamorphism · Monazite dating · Zircon dating

## Introduction

High-pressure metamorphic mineral assemblages are preserved when minerals are unable to re-equilibrate in response to changing *P–T–X* conditions during exhumation (Schliestedt 1986; Ernst 1988; Cuthbert and Carswell 1990;

Rubie 1990; O'Brien and Carswell 1993; Gao et al. 1999; Wallis and Aoya 2000; Carswell et al. 2000; Abbott and Greenwood 2001). The re-equilibration process is commonly attributed to fluid-driven retrogression (Agard et al. 2000) and the presence of reactive lithologies (Spalla et al. 1999; Carswell et al. 2000; Abbott and Greenwood 2001; Gao and Klemd 2001) and takes place via numerous continuous and discontinuous reactions providing pathways by which peak  $P-T$  assemblages are modified during retrogression. However, in rocks comprising minerals with end-member compositions, the number of continuous reactions is greatly reduced, and therefore, fewer pathways are available for the peak  $P$  assemblages to re-equilibrate to post-peak conditions.

High- $P$  metamorphic terranes are keys to understanding collisional orogens and subduction zones. Continental collision- and subduction zones, characterized by high- $P$  metamorphism, are commonly reported from the Proterozoic onwards but rarely recorded in Archean times (Brown 2007). Recent studies e.g., Moyen et al. (2006) have identified Paleoarchean ( $\sim 3.2$  Ga) high- $P$  ( $\sim 14$  kbar, 600–800°C) metamorphism from the Kaapvaal craton. Neoarchean (ca. 2.72 Ga) high- $P$  (14–17 kbar, 740–865°C) metamorphic events have been reported from eclogite blocks in the eastern Belomorian Province in Russia (Brown 2009). The Neoarchean Era is also characterized by ultra-high temperature (UHT) metamorphism (Millonig et al. 2008) marking the onset of duality of thermal regimes commonly inferred for Proterozoic and Phanerozoic subduction zones. These observations support the idea that plate tectonic processes similar to that seen in the Proterozoic were already operational in the Neoarchean and may have been related to the accretion, assembly and breakup of supercontinents in the past.

The Indian peninsula comprises several cratonic blocks i.e., Singhbum, Dharwar, Bundelkhand, and Bastar, which have experienced multiple tectonometamorphic events over protracted periods of time in the Archean. However, excepting a handful of studies e.g., Goswami et al. (1995), Mishra et al. (1999) and Mondal et al. (2002) who have reported 3.3–3.2 Ga upper amphibolite-facies metamorphism from the Bundelkhand and Singhbum cratons, the  $P-T-t$  evolutionary history of these cratonic blocks are poorly constrained compared to other greenstone belts of the world e.g., Barberton and its south in SE Kaapvaal craton (e.g., Moyen et al. 2006) and Isua Supracrustal Belt in West Greenland (Komiya et al. 2002).

In this study, we document for the first time a well-constrained record of Neoarchean ( $>2.73$  Ga) high- $P$  (12–20 kbar) metamorphism from corundum + phlogopite + chlorite + clinozoisite + muscovite + margarite-bearing schists in the Bundelkhand craton (BC) of India. The composition of the rocks closely approaches the model

$\text{Na}_2\text{O}-\text{CaO}-\text{K}_2\text{O}-\text{MgO}-\text{Al}_2\text{O}_3-\text{SiO}_2-\text{H}_2\text{O}$  system. These schists preserve a bi-layered corona at the contact between corundum porphyroblasts and phlogopite + chlorite + clinozoisite-bearing matrix foliation. The outer corona abutting the matrix foliation consists of phengitic-muscovite + chlorite symplectite, whereas the inner corona against corundum consists of muscovite + margarite ± chlorite. The formation of the outer corona preceded the inner one and was synchronous with deformation, which produced crenulations in the matrix foliation. KMASH and CKMASH pseudosection modeling using effective compositions of reaction volume computed from modal abundances and compositions of product phases indicate that the outer phengitic-muscovite + chlorite symplectite-bearing corona and the inner muscovite + margarite-bearing corona formed at 18–20 kbar and ca. 12 kbar, respectively. The rocks were decompressed along a clockwise  $P-T$  path, documenting a Neoarchean collisional tectonic event in the Indian subcontinent.

## Geologic background

The BC exposed over an area of ca. 29,000 km<sup>2</sup> in north central India (Fig. 1a, b) is dominated by Banded Iron Formations, inter-bedded quartzites, calc-silicate gneisses, ultramafic rocks of komatiitic affinity (similar to modern boninites; Malviya et al. 2006), amphibolites, pillow lavas, and volcanoclastic meta-sediments. These units occurring as slivers in variably deformed younger granitoids are inferred to be the remnants of supra-subduction crust tectonically emplaced during Archean arc-continent-continent collision (Malviya et al. 2006). Zircon grains from the basement gneiss-greenstone components yield an ion microprobe  $^{207}\text{Pb}/^{206}\text{Pb}$  age of  $3,270 \pm 3$  Ma (Mondal et al. 2002). An older Rb-Sr whole rock isochron age of  $3,503 \pm 99$  Ma has been reported by Sarkar et al. (1996) for the Baghara trondhjemite gneiss south of Babina. The expansive granitoids in the BC include syeno- and monzogranite, granodiorite, diorite, alkali feldspar syenite, granite porphyry and rhyolite (Rahaman and Zainuddin 1993; Mondal et al. 2002; Pati et al. 2007, 2008a, b). Pb-Pb isochron ages of zircon from these granitoids range from 2,492 to 2,551 Ma in rhyolite/granophyre/granite porphyry and  $2,563 \pm 6$  Ma in diorite (Mondal et al. 2002; Jourdan et al. 2008) and are suggested to be the stabilization age of the craton (Mondal et al. 2002).

The granites are dissected by regional east-west trending sub-vertical sinistral shear zones (Fig. 1c) e.g., Raksa Shear Zone, some  $>50$  m wide (Sentiappan 1976, 1981) close to the  $25^{\circ}15'N$  latitude (Pati 1998, 1999). The last episode of magmatic activity in the craton is manifested by NW-trending mafic dykes post-dating the shear

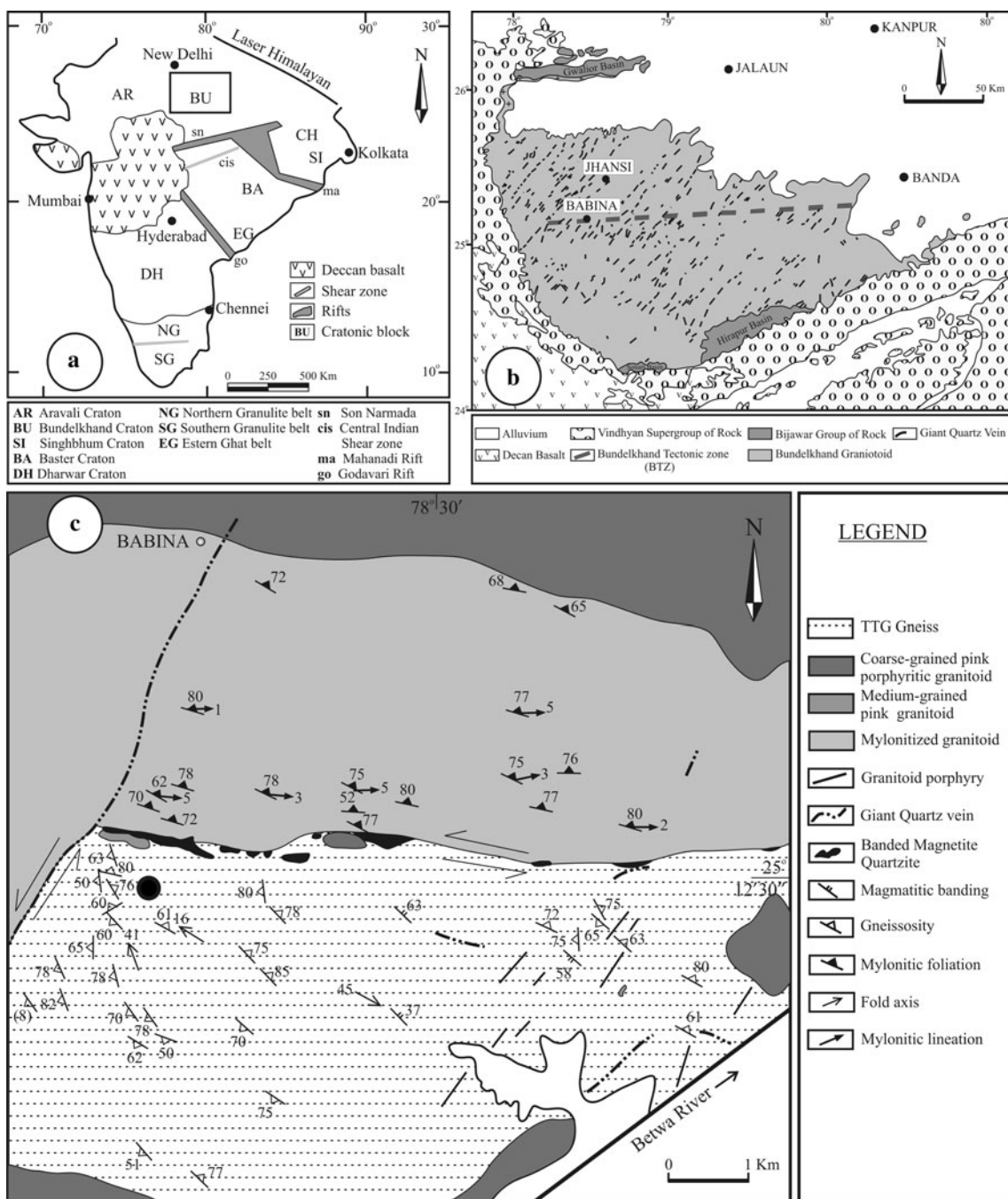


**Fig. 1** **a** A generalized map of India showing the major geological Provinces including the Bundelkhand craton (BC). **b** Geological map of the Bundelkhand craton (simplified after Pati et al. 2007) showing

the location of Babina, near to where the samples come from. **c** Geological map of the area around Babina showing the location of ‘white schist’ samples examined in this study (filled circle)

zones (Basu 1986; Mondal and Ahmad 2001; Pati et al. 2008b). Based on  $^{40}\text{Ar}/^{39}\text{Ar}$  step heating ages, Rao et al. (2005) infer two phases of dyke intrusion at 2,000 and 2,150 Ma. These ages partly overlap with Rb–Sr isochron ages (2,130 and 2,402 Ma) from granitoids and tonalite-trondjemite-granodiorite (TTG) suites (Sarkar et al. 1994). The metamorphic evolution of the Bundelkhand craton is poorly constrained. Basu (1986) reported

greenschist to amphibolite facies conditions for the basement gneisses and schists, whereas Singh et al. (2007) and Singh and Dwivedi (2009) inferred granulite facies condition with peak  $P-T$  of 730°C and 5.4 kbar for cordierite-garnet-sillimanite-quartz metapelites intruded by 3.2–3.4 Ga old TTG.

The quartz-free white-colored schists (Fig. 2a) described in this study occur in a 2 m<sup>2</sup> elliptical outcrop in the

Chaurara Reserve Forest (Survey of India topographic sheet no. 54 K/8-NE) south of Babina,  $25^{\circ}12'30.4''\text{N}$  latitude,  $78^{\circ}27'55.1''\text{E}$  longitude. The contact relations between the schist and the surrounding rocks are obscured by poor exposure conditions of the rocks.

## Petrography and whole rock chemistry

The dominant minerals in the schists include interleaved phlogopite and chlorite defining a crenulated continuous foliation (Fig. 2a). Corundum occurs as isolated porphyroblasts wrapped around by the phlogopite + chlorite defined fabric (Fig. 2b, c). Clinzoisite locally occurs within the matrix foliation (Fig. 2b, d). The corundum porphyroblasts, largely free of mineral inclusions, are mantled by thin ( $<100\ \mu\text{m}$ ) collars of margarite intergrown with muscovite (Figs. 2b, c, 3a, b). Incursions of inter-grown margarite + muscovite into corundum are frequent (Fig. 2b, c), and strongly embayed corundum commonly occurs as rafts within the margarite + muscovite collars (Figs. 2b, c, 3a, b). The inner collars are

mantled by wider ( $>250\ \mu\text{m}$ ) outer collars of fine-grained ( $<3\ \mu\text{m}$  wide) muscovite + chlorite symplectite, which are locally axial planar to crenulations of the matrix foliation (Fig. 2b, c). Flakes of matrix phlogopite are commonly stranded within the outer corona layer (Fig. 3a, b). This feature is absent in the margarite + muscovite layer. The margarite + muscovite coronal layer around corundum rarely occurs exclusive of the muscovite + chlorite layer (Fig. 3), but the muscovite + chlorite outer corona exclusive of margarite-bearing layer is infrequent (arrow with bar, Figs. 2, 3). This suggests that the corona-forming reactions may be different for the margarite + muscovite and muscovite + phlogopite layers. Monazite and zircon are the two common accessory phases in the rock. Both minerals occur in the phlogopite + chlorite matrix as well as in the margarite + muscovite and margarite + muscovite + chlorite corona mantling corundum. Zircon also occurs as corundum-hosted inclusions.

The schists have high  $\text{Al}_2\text{O}_3$  (17–22 wt%),  $\text{MgO}$  (25–27 wt%), and  $\text{H}_2\text{O}$  (7–10 wt% as loss on ignition (Table 1; see electronic supplementary material for analytical methods). Their bulk  $\text{H}_2\text{O}$  content is bracketed by

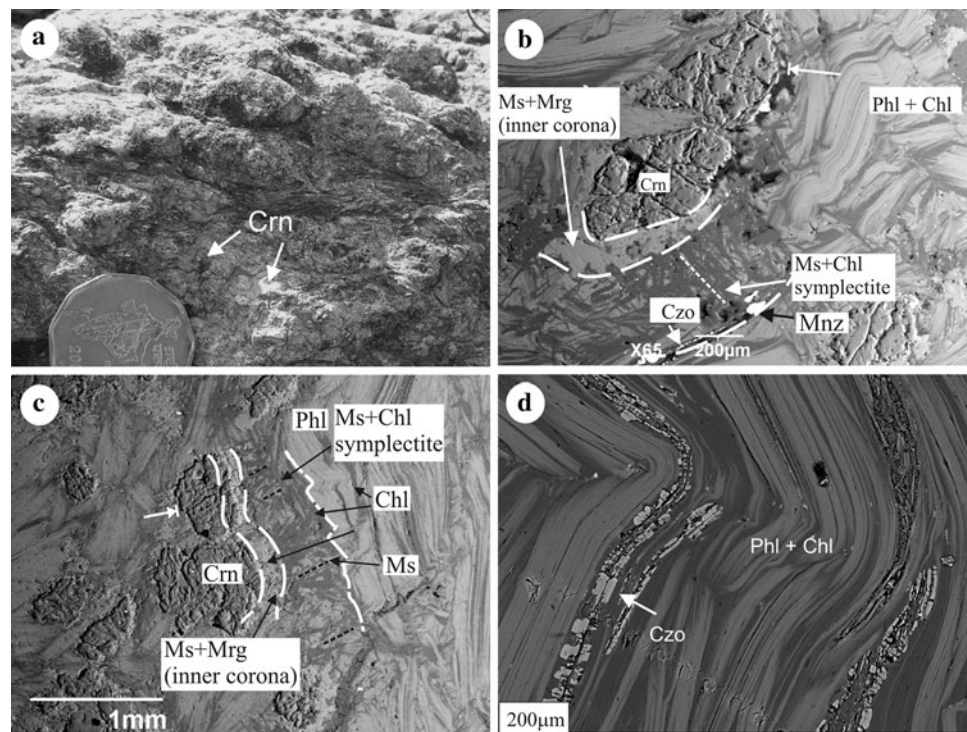


**Fig. 2** Field photograph (a) and BSE images (b–d) of chlorite-phlogopite-corundum schists from the Babina area (Fig. 1). **a** Close-up view showing colorless post-tectonic corundum (Crn) porphyroblasts (coin diameter 2.5 cm) in schists showing crenulated phlogopite (Phl)-chlorite (Chl)-defined foliations. **b, c** Embayed corundum porphyroblasts mantled by bi-layered corona post-tectonic with respect to phlogopite-chlorite defined early (penetrative) foliation. Dotted line indicates local orientation of the muscovite-chlorite symplectite axial

planar to crenulations on the early foliation. Broken lines demarcate the boundaries between corundum, margarite–muscovite inner corona, muscovite–chlorite outer corona and the phlogopite–chlorite matrix. Arrow with bar identifies locations in the coronal zones around corundum where the margarite–muscovite inner layer is either absent or very thin. **d** Layers of clinzoisite (Czo), with transverse fractures, inter-leaved with phlogopite–chlorite in the schist. Mineral abbreviations used in this and following figures are after Kretz (1983)

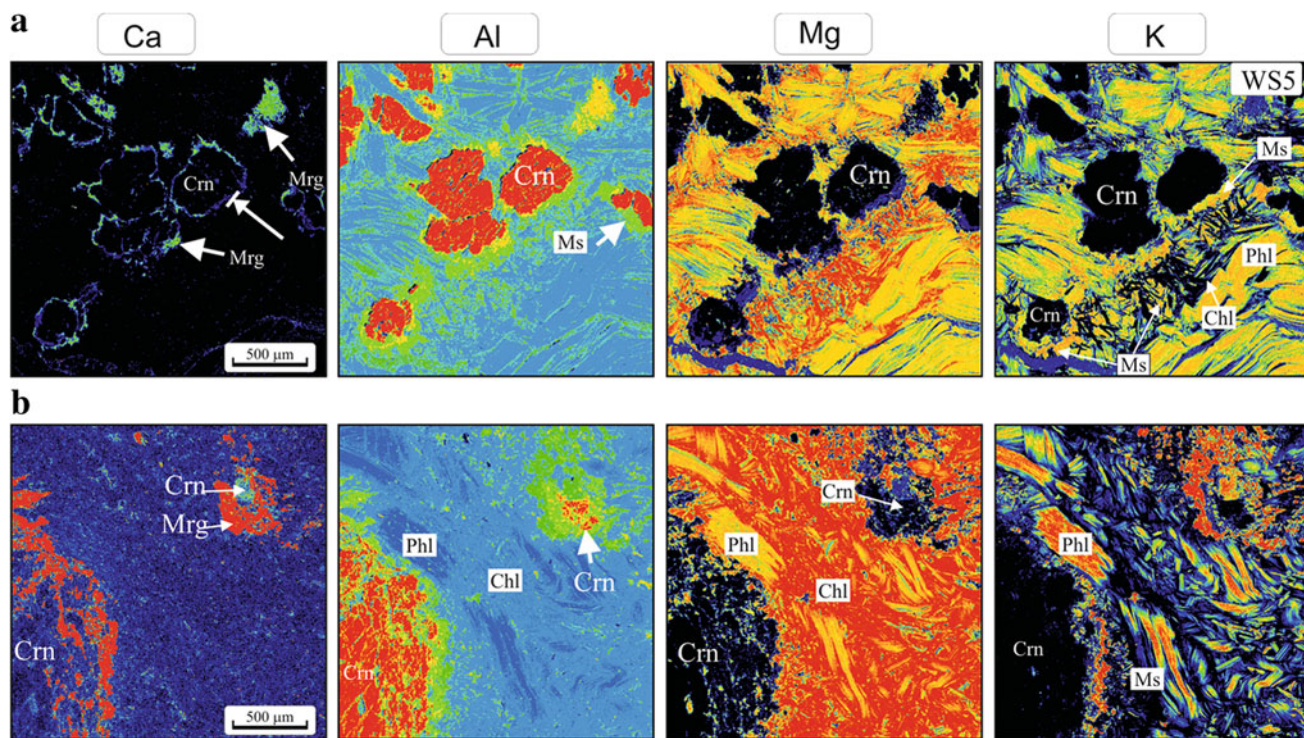


**Fig. 3** X-ray element (Ca, Al, Mg, K) images showing bi-layered corona (see text) mantling corundum porphyroblasts in two schist samples **a** top-set (WS-5) and **b** bottom set (WS-2). The compositional variations across the corona in the bottom set images along

A–B and C–D traverses is shown in Fig. 5. Arrow with bar in the top-left Ca image shows margarite layer neighboring the corundum porphyroblast is absent, although the phlogopite–chlorite corona is evident

**Table 1** Whole rock XRF major element oxide concentrations (wt%) and loss on ignition (LOI) of chlorite–phlogopite–corundum schists, and profile analyses used for P–X pseudosections (in Fig. 7)

	Whole rock XRF (wt%)			Profile data used for P–X pseudosection in wt% (Fig. 7)	
	WS-2	WS-3	WS-4	C1	C2
SiO <sub>2</sub>	39.19	39.62	39.81	19.93	30.38
TiO <sub>2</sub>	0.37	0.35	0.47	0.03	0.04
Al <sub>2</sub> O <sub>3</sub>	17.44	22.09	17.79	64.41	23.69
Fe <sub>2</sub> O <sub>3</sub> <sup>a</sup>	0.71	0.73	0.85	n.a.	n.a.
FeO	n.a.	n.a.	n.a.	0.10	0.63
MnO	0.05	0.05	0.07	0.00	0.00
MgO	26.80	26.29	25.61	0.83	29.73
CaO	0.38	0.68	0.19	5.65	0.00
Na <sub>2</sub> O	0.25	0.25	0.18	0.65	0.02
K <sub>2</sub> O	5.07	4.05	7.20	0.74	1.78
P <sub>2</sub> O <sub>5</sub>	0.01	0.01	0.01	n.a.	n.a.
LOI	10.39	7.23	8.55		
Total	101	101	101		
X <sub>Mg</sub>	0.99	0.99	0.98	0.94	0.99

<sup>a</sup> Total Fe as Fe<sub>2</sub>O<sub>3</sub>

the structurally held H<sub>2</sub>O contents in muscovite/biotite (ca. 3.8 wt%) and chlorite (ca. 12.5 wt%), the two dominant mica group of minerals in the rocks. The K<sub>2</sub>O content varies between 5 and 7 wt%. Total Fe as Fe<sub>2</sub>O<sub>3</sub>

varies between 0.7 and 0.8 wt%, and the CaO content is in the range of 0.2–0.7 wt%. MnO, TiO<sub>2</sub>, and P<sub>2</sub>O<sub>5</sub> abundances are very low and together constitute <0.5 wt% of the rock.

**Table 2** Representative microprobe analyses of phlogopite

Spot no.	Matrix							Relict within Phe-Chl symplectite domain						
	WS5					WS2			WS5			WS2		
	6 Core	9	21	27 Rim	28	5 Core	13	15	31	32	33	43	44	49
SiO <sub>2</sub>	39.27	40.18	40.45	38.73	39.87	39.15	40.08	39.04	37.11	37.57	37.42	38.6	37.8	39.15
TiO <sub>2</sub>	0.46	0.47	0.49	0.43	0.5	0.39	0.39	0.42	0.31	0.36	0.4	0.4	0.36	0.45
Al <sub>2</sub> O <sub>3</sub>	18.99	19.56	19.47	20.02	19.66	20.29	18.8	19.6	22.13	22.7	22.94	20.62	21.24	21.67
Cr <sub>2</sub> O <sub>3</sub>	0	0	0	0	0.01	0.02	0.02	0	0.08	0.1	0.01	0.05	0.03	0
FeO	0.61	0.54	0.74	0.70	0.65	0.47	0.48	0.59	0.70	0.65	0.77	0.60	0.56	0.59
MnO	0.08	0.04	0.07	0.1	0.1	0	0	0	0.12	0.06	0.11	0	0.05	0
MgO	23.73	23.72	23.64	23.4	23.74	23.16	23.81	23.55	23.08	23.55	23.72	23.96	24.47	24.16
CaO	0	0	0	0	0	0	0	0	0	0.01	0	0	0	0
Na <sub>2</sub> O	0.05	0.16	0.12	0.04	0.06	0.1	0.1	0.08	0.06	0.04	0.05	0.18	0.09	0.1
K <sub>2</sub> O	9.98	9.25	9.48	10.24	10.16	9.89	9.55	9.26	8.56	8.54	8.76	9.28	8.48	9.19
Total	93.19	93.94	94.48	93.67	94.77	93.48	93.24	92.55	92.16	93.6	94.19	93.7	93.09	95.32
X <sub>Phl</sub>	0.77	0.77	0.77	0.76	0.76	0.75	0.77	0.76	0.73	0.73	0.73	0.75	0.75	0.75
X <sub>East</sub>	0.23	0.23	0.23	0.24	0.24	0.25	0.23	0.24	0.27	0.27	0.27	0.25	0.25	0.25
X <sub>Mg</sub>	0.99	0.99	0.99	0.99	0.99	0.99	0.99	0.99	0.99	0.99	0.98	0.99	0.99	0.99

**Mineral chemistry**

Electron probe micro analytical (EPMA) data of minerals are listed in Tables 2, 3, 4 and relevant compositional variations illustrated in Fig. 4a, b. Details of the analytical techniques are provided in the electronic supplementary material.

**Phlogopite**

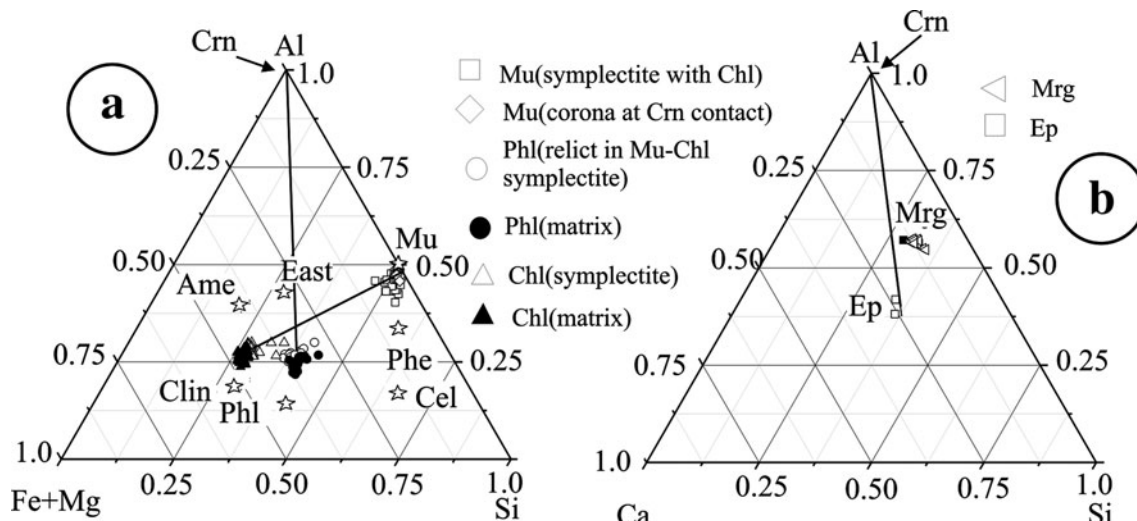
The composition of biotite lies on the phlogopite–eastonite join (Fig. 4a; data in Table 2). In sample WS5, Al<sub>(IV)</sub> in matrix phlogopite increases from core (1.19–1.22 p.f.u.) to rim (1.22–1.26 p.f.u.) against the muscovite + chlorite symplectite domain. In WS2, Al<sub>(IV)</sub> in matrix phlogopite

**Table 3** Representative microprobe analyses of muscovite and margarite

Spot no.	Ms-Chl symplectite							Ms-Mrg corona							
	WS5					WS2			WS5			WS2		WS5	
	37 Muscovite	55	43	18	78	31 Muscovite	41	59	54	36	76 Muscovite	88	94	15	31 Margarite
SiO <sub>2</sub>	44.8	50.08	45.68	50.05	49.63	47.59	47.72	50.45	48.03	46.28	49.2	49.38	49.01	31.23	32.72
TiO <sub>2</sub>	0.24	0.32	0.78	0.06	0	0.07	0.26	0.36	0.58	0.58	0	0.35	0.23	0	0
Al <sub>2</sub> O <sub>3</sub>	35.12	31.65	33.05	34.98	35.58	34.5	37.7	33.83	33.61	36.42	37.11	37.19	37.71	50.15	48.86
Cr <sub>2</sub> O <sub>3</sub>	0	0	0	0.03	0	0	0	0	0	0.06	0	0.03	0.01	0	0
FeO	0.269	0.111	0.102	0.223	0.11	0.093	0.113	0.11	0.102	0.08	0	0.02	0.158	0	0.02
MnO	0.04	0	0	0	0	0	0	0.01	0	0.04	0.15	0	0.03	0.02	0.12
MgO	3.22	3.44	3.74	2.25	1.28	3.97	1.2	2.33	2.75	0.94	0.67	0.87	0.72	0.09	0.17
CaO	0.16	0.01	0	0.25	0.02	0.12	0	0	0	0	0	0.04	0	12.7	10.61
Na <sub>2</sub> O	0.15	0.09	0.09	0.15	0.14	0.1	0.37	0.19	0.21	0.29	0.38	0.32	0.36	0.62	1.16
K <sub>2</sub> O	10.57	10.43	10.09	8.48	9.46	8.66	10.32	10.82	10.11	10.17	9.51	9.34	8.92	0.07	0.83
Total	94.59	96.14	93.54	96.47	96.22	95.1	97.68	98.1	95.39	94.86	97.02	97.54	97.15	94.88	94.49
X <sub>Prg</sub>	0.02	0.01	0.01	0.03	0.02	0.02	0.05	0.03	0.03	0.04	0.06	0.05	0.06	0.08	0.15
X <sub>Mrg</sub>	0.01	0.00	0.00	0.02	0.00	0.01	0.00	0.00	0.00	0.00	0.00	0.00	0.00	0.91	0.77
X <sub>Ms</sub>	0.97	0.99	0.99	0.95	0.98	0.97	0.95	0.97	0.97	0.96	0.94	0.95	0.94	0.01	0.07
X <sub>Phengite</sub>	0.54	0.60	0.57	0.56	0.55	0.57	0.53	0.57	0.57	0.53	0.53	0.54	0.53		

**Table 4** Representative microprobe analyses of chlorite and zoisite

Spot no.	Chl-Matrix							Chl in symplectite						Zo (Matrix)
	7 WS5	8	39	40	21 WS2	28	32	27 WS5	44	113	44 WS2	40	52	7 WS2
SiO <sub>2</sub>	28.8	29.76	31.15	30.51	29.82	28.45	27.9	29.1	29.84	29.77	29.06	28.87	28.67	39.13
TiO <sub>2</sub>	0.01	0	0.03	0.04	0	0.07	0	0.06	0.04	0	0	0.04	0.05	0.04
Al <sub>2</sub> O <sub>3</sub>	24.89	23.24	22.53	23.15	23.51	25.15	25.57	24.36	22.76	23.2	23.76	25.03	25.43	31.44
Cr <sub>2</sub> O <sub>3</sub>	0	0	0.04	0.01	0	0	0.03	0	0	0	0.02	0	0	0
FeO	0.84	0.63	0.74	0.78	0.58	0.76	0.81	0.74	0.71	0.81	0.62	0.49	0.67	1.32
MnO	0.12	0	0.09	0.11	0.08	0.06	0	0.12	0.14	0	0	0.09	0	0.01
MgO	31.83	31.91	30.74	31.37	31.96	31.43	31.37	31.65	32.86	31.57	30.86	29.97	30.04	0.05
CaO	0.03	0	0.02	0.07	0	0	0	0	0.02	0.01	0	0.02	0.12	24.59
Na <sub>2</sub> O	0	0	0.03	0	0.01	0.02	0.01	0	0	0.03	0.03	0.04	0.07	0.05
K <sub>2</sub> O	0.14	0	0.77	0.2	0.06	0.03	0	0.15	0.03	0.02	0.02	0.52	0.08	0.02
Total	86.66	85.54	86.14	86.24	86.02	85.97	85.69	86.18	86.4	85.41	84.37	85.07	85.13	96.65
X <sub>Mg</sub>	0.985	0.990	0.987	0.986	0.990	0.987	0.986	0.987	0.988	0.986	0.989	0.991	0.988	

**Fig. 4** Ternary chemographic plots of measured compositions (Tables 2, 3, 4) of phlogopite, muscovite, chlorite margarite and clinozoisite in texturally different domains (see text) in **a** Al-(Fe + Mg)-Si diagram and **b** Al-Ca-Si diagram

varies in the range 1.18–1.24 p.f.u. In WS5, the Al<sub>(VI)</sub> content of core (0.370–0.415 p.f.u.) and rim (0.393–0.405 p.f.u.) matrix-phlogopite overlap. In WS2, Al<sub>(VI)</sub> in matrix phlogopite varies from 0.386 to 0.443 (p.f.u.). The X<sub>East</sub> of matrix phlogopite in WS5 shows no variation from core (0.24) to rim (0.23) against muscovite + chlorite symplectite and are similar to the values of X<sub>East</sub> (0.23–0.25) in matrix phlogopite from WS2. Phlogopites from the symplectite domains in both WS2 and WS5 have higher Al<sub>(IV)</sub> and Al<sub>(VI)</sub> contents than those in the matrix. In WS5, Al<sub>(IV)</sub> content of phlogopite from the symplectite domains varies between 1.36 and 1.39, whereas Al<sub>(VI)</sub> content varies

from 0.494 to 0.502. In WS2, Al<sub>(IV)</sub> content of phlogopite from symplectite domains varies between 1.29 and 1.34 and Al<sub>(VI)</sub> content varies from 0.417 to 0.454. The X<sub>East</sub> of phlogopite from muscovite + chlorite symplectite domains in WS5 and WS2 are ca. 0.27 and ca. 0.25, respectively. The X<sub>Mg</sub> of matrix- and symplectite-phlogopite in both WS2 and WS5 is ca. 0.99.

#### Muscovite

Muscovite from both outer symplectite layer and inner corona is phengitic (Fig. 4a; data in Table 3). The Mg, Si,

and Al (total) contents of the symplectitic muscovite range from 0.123 to 0.376 (p.f.u), 3.00 to 3.27 (p.f.u) and 2.43 to 2.77 (p.f.u), respectively in WS5, and 0.193–0.387 (p.f.u), 3.06–3.23 (p.f.u) and 2.55–2.85 (p.f.u), respectively in WS2. Mg, Si and Al (total) content of muscovite in the muscovite–margarite coronal layer ranges from 0.064 to 0.083 (p.f.u), 3.13–3.15 (p.f.u) and 2.79–2.84 (p.f.u), respectively in WS5. The  $X_{\text{Phengite}}$  of muscovite from the inner corona (ca. 0.53) in WS5 is slightly lower than that of the symplectite muscovite (0.55–0.60).

#### Margarite

Margarite in both samples WS2 and WS5 contains 8–17 mol% paragonite in solid solution (Table 3).

#### Chlorite

Matrix and symplectite-chlorite are compositionally similar and are solid solutions between clinochlore and amesite (average composition: 27% amesite, 83% clinochlore; (Fig. 4a; Table 4). The  $X_{\text{Mg}}$  of matrix- and symplectite-chlorite is ca. 0.99.

#### Clinzoisite

The  $\text{Fe}^{2+}$  and Al content of clinzoisite is ca. 0.085 (p.f.u) and ca. 2.87 (p.f.u.), respectively (Table 4).

### Corona-forming reactions

The presence of an inner collar of muscovite + margarite and an outer collar of muscovite + chlorite around corundum porphyroblasts (Figs. 2b, c, 3a, b) suggests that these assemblages formed by reactions between corundum and the matrix phlogopite + chlorite  $\pm$  clinzoisite. The oriented growth (axial planar to crenulations) of the muscovite + chlorite in the outer collar (Fig. 2b, c) indicates that corona formation was synchronous with deformation that produced the crenulations in the matrix foliation. In the inner collar, muscovite and margarite show no preferred orientation. One possible explanation for this is that the inner corona postdates the deformation vis-à-vis the formation of the outer coronal layer.

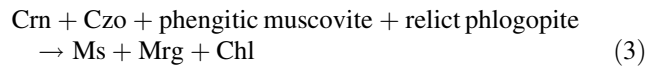
Tie-line intersection in Fig. 4a suggests the following KMASH reaction for the formation of muscovite + chlorite symplectite in the outer coronal layer:



In Ca–Al–Si diagram (Fig. 4b), margarite plots close to the corundum–clinzoisite binary join suggesting that margarite may have formed by the CASH reaction:



Although clinzoisite is not observed in direct contact with corundum, it is considered a likely reactant phase since it is the only Ca-bearing mineral in the matrix, barring monazite. Possibly, reaction (2) was initiated wherever clinzoisite–corundum occurred together and led to the total consumption of clinzoisite at the contact with corundum. However, this reaction does not explain the muscovite (and minor chlorite) associated with margarite, and the ca. 8–17 mol% paragonite in solid solution with margarite. The possible source of the paragonite component in margarite is phengitic-muscovite in the outer collar. Therefore, the formation of muscovite and margarite with minor chlorite in the inner corona can be explained by a reaction involving corundum–clinzoisite aggregates along with phengitic muscovite of the outer collar and relict phlogopite:

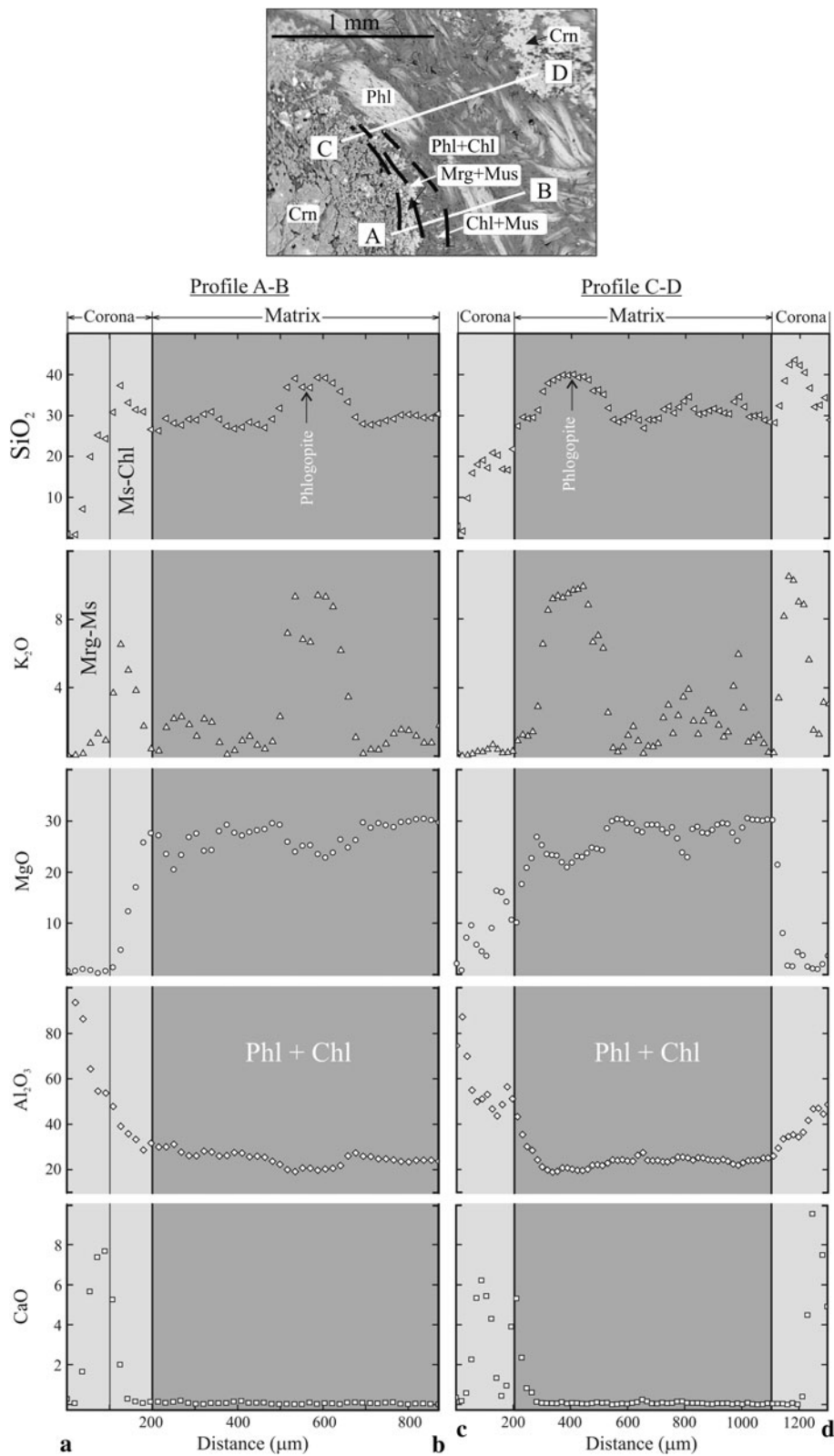


Margarite is stable at  $P \leq 10$  kbar (Chatterjee 1976; Gibson 1979). At high pressures, clinzoisite is the stable phase (Chatterjee 1976). Given the low negative  $dP/dT$  slopes of the reactions  $\text{Mrg} + \text{Qtz} \rightarrow \text{Cz} + \text{Ky} + \text{Pg} + \text{H}_2\text{O}$  (CASH system) and  $\text{Mrg}_{\text{ss}} + \text{Qtz} \rightarrow \text{Cz} + \text{Ky} + \text{Pg}_{\text{ss}} + \text{H}_2\text{O}$  (NCASH system) (Chatterjee 1976), the formation of margarite at the expense of clinzoisite involves decompression (Faryad and Hoinkes 2006). This observation, coupled with the higher eastonite content (i.e. higher Al content) of relict phlogopite from the muscovite + chlorite domain relative to the rim of matrix phlogopite in WS5 (Tables 2, 3, 4), is indicative of decrease in pressure (Vidal and Parra 2000). In summary, it appears that the phengitic-muscovite + chlorite collar formed earlier at a higher pressure (reaction 1) and was followed by the stabilization of lower pressure margarite + muscovite assemblage in the inner collar along an inward retreating margin of the consuming corundum porphyroblast.

### Chemical variation across corona and corona formation mechanism

The major element compositional variation across the double-layered corona mantling corundum was estimated by analyzing line profiles with ca. 18  $\mu\text{m}$  overlap between spots using a wide (50  $\mu\text{m}$ ) diameter electron beam on an EPMA (details of analytical technique are provided in the electronic supplementary material). Figure 5 illustrates the variation in K, Ca, Mg, Al, and Si across the two coronal layers.  $\text{Al}_2\text{O}_3$  decreases sharply from the margin of

**Fig. 5** Major element oxide variations across coronal layers along traverses A–B and C–D (BSE image at top, and bottom set Ca, Al, Mg, and K images in Fig. 3). Broken lines demarcate the boundaries between corundum, margarite–muscovite inner corona, muscovite–chlorite outer corona, and phlogopite–chlorite matrix. Each point represents the composition of micro-domains analyzed with 50- $\mu\text{m}$ -wide beam diameter of electron probe micro analyzer. The distance between successive beam centers along the profiles is ca. 18  $\mu\text{m}$



corundum to ca. 30 wt% within the corona (Fig. 5), before flattening out at 20–23 wt% in the phlogopite + chlorite matrix. The high-Al content in the muscovite + margarite

zone is partly due to the presence of un-reacted corundum grains stranded within the inner collar (Fig. 3). MgO concentrations are low in the inner collar, indicating the

near-absence of Fe–Mg micas, such as chlorite and phlogopite. The decrease in  $\text{Al}_2\text{O}_3$  in the margarite + muscovite zone is associated with increase in  $\text{CaO}$  and  $\text{SiO}_2$  (increase in  $\text{SiO}_2 > \text{CaO}$ ), followed by  $\text{K}_2\text{O}$  some distance inwards into the margarite + muscovite zone. This indicates that muscovite and margarite are somewhat segregated and not uniformly distributed (Fig. 3). From the margarite–muscovite inner collar toward the phengitic muscovite–chlorite outer collar,  $\text{CaO}$  abundances decrease to zero, whereas  $\text{MgO}$  continues to increase. Beyond this zone,  $\text{K}_2\text{O}$  and  $\text{SiO}_2$  both reach highs followed by a slump as the phengitic-muscovite + chlorite zone is reached. Within the  $\text{CaO}$  hump, which coincides with the margarite + chlorite inner corona,  $\text{MgO}$  increases marginally, while  $\text{K}_2\text{O}$  is low. At the point where  $\text{CaO}$  is at its lowest,  $\text{K}_2\text{O}$  and  $\text{MgO}$  increase sharply, whereas  $\text{SiO}_2$  abundance dips marginally. Beyond this point toward the matrix, element abundances remain broadly constant, barring a small zone where both  $\text{SiO}_2$  and  $\text{K}_2\text{O}$  increase, with a complementary decrease in  $\text{MgO}$ . This zone corresponds to phlogopite-rich part of the matrix. The chemical gradients across the corona are sharper than is depicted in Fig. 5 because the ca. 18  $\mu\text{m}$  overlap between the centers of adjacent 50  $\mu\text{m}$  diameter electron beam cause the chemical gradients to smear over distances larger than they actually are.

The transport of elements to thermodynamically unstable, reactive corona-forming zones takes place by two processes operating independently or in tandem, e.g., (a) molecular diffusion whereby local chemical gradients cause element transport (Fisher and Elliott 1974) and (b) advection in which conserved elements are transported as scalar quantities in moving fluids (Lichtner 1988; Ashworth and Sheplev 1997; Fisher and Lasaga 1981; Balashov and Lebedeva 1991). Though the increase in Si and Mg and the decrease in Al outward from corundum in the corona can be explained by both diffusion as well as advective transport, the Ca spike (due to presence of margarite) in the inner coronal layer is difficult to explain by advective diffusion alone because the matrix minerals (phlogopite and chlorite) and corundum contain negligible Ca. Possibly, the inner corona formed by local diffusive element transport and reaction between the matrix minerals and corundum and a Ca-bearing pre-coronal phase, presumably clinzoisite alongside corundum. The sharp chemical gradients in the corona, the simple mineralogy of the individual coronal layers (Ashworth and Sheplev 1997), the lack of within-corona repetitive layering (Fisher and Lasaga 1981) possibly suggest that corona formation was induced by ‘molecular diffusion’ (Fisher and Elliott 1974; Ashworth et al. 1992) across interfaces of pre-coronal phase boundaries.

## P–T conditions of corona formation

The mineralogically layered corona may also be interpreted to form by a single reaction instead of multiple reactions, with the Mg-poor, Al-richer product phases (muscovite-margarite) forming the inner collar adjacent to the Al-saturating phase corundum and the Mg-rich Al-poorer product phases (phengitic-muscovite + chlorite) forming the outer collar adjacent to the ferromagnesian matrix of phlogopite + chlorite. If all four product phases formed through a single reaction, then the P–T condition for corona formation retrieved using reactions involving phase components of the four phases and the reactants (corundum, zoisite, phlogopite and chlorite) should be similar or at least comparable. The plausibility of this hypothesis is tested in the following paragraphs.

P–T conditions of formation of the outer muscovite-chlorite symplectite-bearing reaction rim in sample WS5 is estimated by the intersection of stable reactions between reactants (corundum and phlogopite) and product (muscovite + chlorite symplectite) phases using compositions of muscovite and chlorite from the symplectite domain in equilibrium with the rim of matrix phlogopite. The method is similar to the average P–T method estimation in THERMOCALC. Phase components with low activity (ca. 0.02–0.04), like celadonite, were excluded from the computations. All calculations were performed by THERMOCALC (ver. 3.25). Compositions of the relict phlogopite within the muscovite + chlorite symplectite domains were not used in the computation because the higher eastonite content of these phlogopites suggests that they may have re-equilibrated. For sample WS2, the P–T conditions during the formation of the muscovite-chlorite corona layer was calculated using the composition of muscovite-chlorite and relict phlogopite from the symplectite domain since these phlogopites do not show compositional re-equilibration of their eastonite contents. For both samples, calculations were done for two sets of muscovite-chlorite-phlogopite compositions, and the results are shown in Table 5 and illustrated in Fig. 6. Peak P–T conditions for the muscovite-chlorite layer obtained from WS5 is

**Table 5** P–T conditions for the formation of outer collar estimated based on convergence of stable reactions calculated using the THERMOCALC program (ver 3.25)

Sample no.	Mineral assemblage	Pressure (kbar)	Temperature (°C)
WS5	Phl(28)-Ms(55)-Chl(27)	18.7	620
WS5	Phl(27)-Ms(43)-Chl(44)	18.0	620
WS2	Phl(49)-Ms(31)-Chl(40)	17.0	640
WS2	Phl(43)-Ms(41)-Chl(44)	18.3	630

T values rounded to the nearest ten

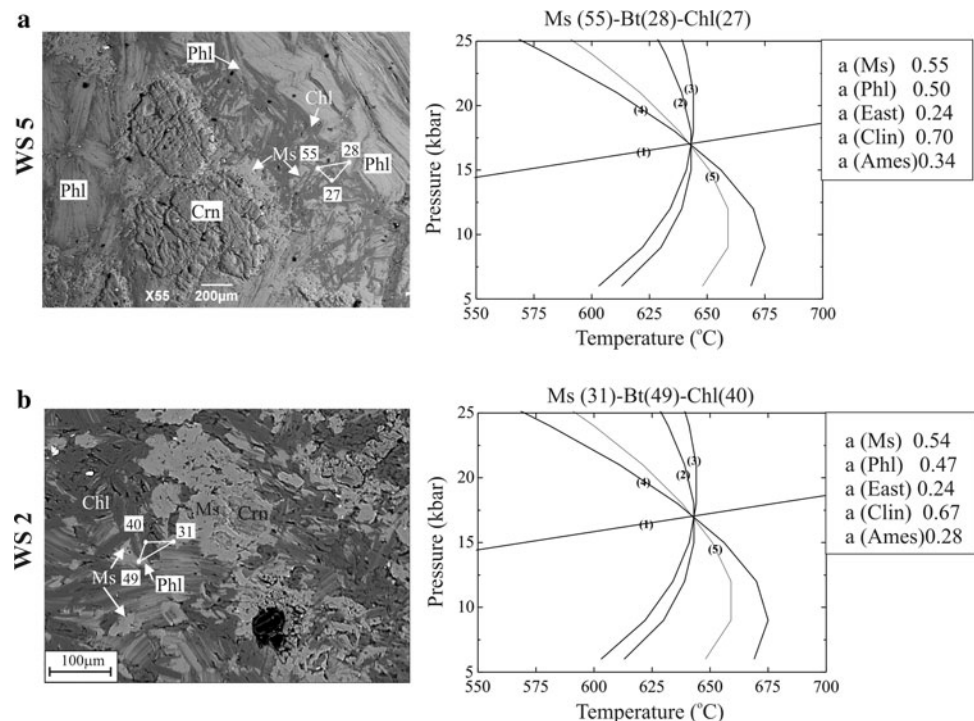


**Fig. 6** Estimates of P-T conditions for the outer (phengitic-muscovite + chlorite) coronal layer mantling corundum in WS 5 (top set a) and WS 2 (bottom set b). Locations of analyzed points used in P-T estimation are keyed to the respective BSE images. Activities of relevant phase components were obtained from the A-X program (Holland and Powell 1998) for the analytical data presented in Tables 2, 3, 4. The numbered reactions are as follows:

(1) phlogopite + amesite = eastonite + clinochlore (2) 9 eastonite + 2 muscovite + 3 clinochlore = 1phlogopite + 14corundum + 12H<sub>2</sub>O (3) 6 eastonite + 2 muscovite + 3 amesite = 8 phlogopite + 14 corundum + 12 H<sub>2</sub>O (4) 2 muscovite + 9 amesite = 2 phlogopite + 6 clinochlore + 14 corundum + 12 H<sub>2</sub>O (5) 2 muscovite + 11 amesite = 2 eastonite + 8 clinochlore + 14 corundum + 12 H<sub>2</sub>O

18–18.7 kbar and 620°C and that from WS2 is 17–18.3 kbar, 630–640°C (Fig. 6, Table 5).

P-T conditions of margarite–muscovite inner coronal layer in WS5 were computed using relict phlogopite in the corona and chlorite at the contact of inner corona in textural equilibrium using the THERMOCALC ver. 3.25 program. The following independent reactions were chosen: (1) phlogopite + amesite = eastonite + clinochlore, (2) 17phlogopite + 48margarite = 3eastonite + 9clinochlore + 14muscovite + 34corundum + 24zoisite, and (3) 10phlogopite + 36margarite = 6clinochlore + 10muscovite + 29corundum + 18zoisite + 3H<sub>2</sub>O. Since no stable reaction involving paragonite component in margarite is obtained, activity of margarite used for the calculation is considered to be 1.0. Average P-T values obtained is 11.8 ± 0.6 kbar (1 SD), and 633 ± 21°C (1 SD).

### P-T conditions from pseudosection analyses

To further constrain the P-T conditions of formation of the coronal layers, P-X and P-T pseudosections were constructed for the KMASH and NCKMASH systems. FeO

and TiO<sub>2</sub> were excluded for the following reasons: (1) X<sub>Mg</sub> of the whole rock (Table 1) is ca. 0.98, (2) the compositions of all ferromagnesian minerals are close to Mg end-members (e.g., phlogopite, clinochlore, Tables 2, 3, 4), (3) absence of Fe<sup>3+</sup> and Ti in phlogopite (Tables 2, 3, 4), (4) the absence of phases like spinel, ilmenite that demonstrably fractionate Fe<sup>3+</sup> and/or Ti. The pseudosections were constructed using the Perple\_X software (Connolly 2005). The mixing properties of mineral phases used for pseudosection modeling are as follows: biotite and orthopyroxene (Powell and Holland 1999), chlorite (Holland et al. 1998), garnet (Holland and Powell 1998), potash feldspar (Thompson and Waldbaum 1969), margarite-paragonite (Frank 1983). For muscovite, the phengite solution model of Holland and Powell (1998) was chosen for P-T pseudosections. For muscovite, the mica (CH1) solution model of Coggan and Holland (2002) was used. H<sub>2</sub>O was taken to be in excess.

### NCKMASH P-X pseudosection

Because the temperatures estimated for the formation of the coronal layers are tightly constrained e.g., 620–640°C

(Fig. 5a, b), isothermal ( $630^{\circ}\text{C}$ ) NCKMASH P–X pseudosections (Fig. 7a, b) were constructed to examine the topology of phase relations as functions of pressure (5–30 kbar) and varying micro-domain compositions following the approach of White et al. (2002). The end-member micro-domain compositions C1 and C2, respectively represent the mean composition of the domain adjacent to corundum porphyroblast and the average composition of the phlogopite-chlorite matrix, estimated from the beam profile data (Table 1; Fig. 5). The modes of corundum, phlogopite, chlorite, phengite, margarite and clinzoisite are also shown in Fig. 7a, b.

Phlogopite–chlorite–phengite bearing assemblages occur at bulk compositions close to C2 in the pressure range of 15–19 kbar (Fig. 7a). Phengite is stable at ca. 15 kbar, its mode increasing with increase in pressure till about 19 kbar (path A–B). Increase in pressure leads to

increase in chlorite and decrease in phlogopite modes indicating that phengitic-muscovite + chlorite-bearing assemblage in the reaction rim was formed with progressive increase in pressure to ca. 19 kbar (Fig. 7b). Thus, the peak pressure for the phengitic-muscovite + chlorite-bearing assemblage may be constrained at ca. 19 kbar.

Corundum–margarite–muscovite–clinzoisite bearing assemblages occur in composition domains close to C1 (Fig. 7a). With progressive decompression, clinzoisite and corundum mode decrease (Fig. 7b). Along this path, margarite modes are closely spaced at about 12 kbar, indicating margarite formation at the expense of corundum and clinzoisite at around this pressure (Fig. 7b). By implication, margarite formed at about 12 kbar at the expense of clinzoisite and corundum, clinzoisite being completely reacted out.

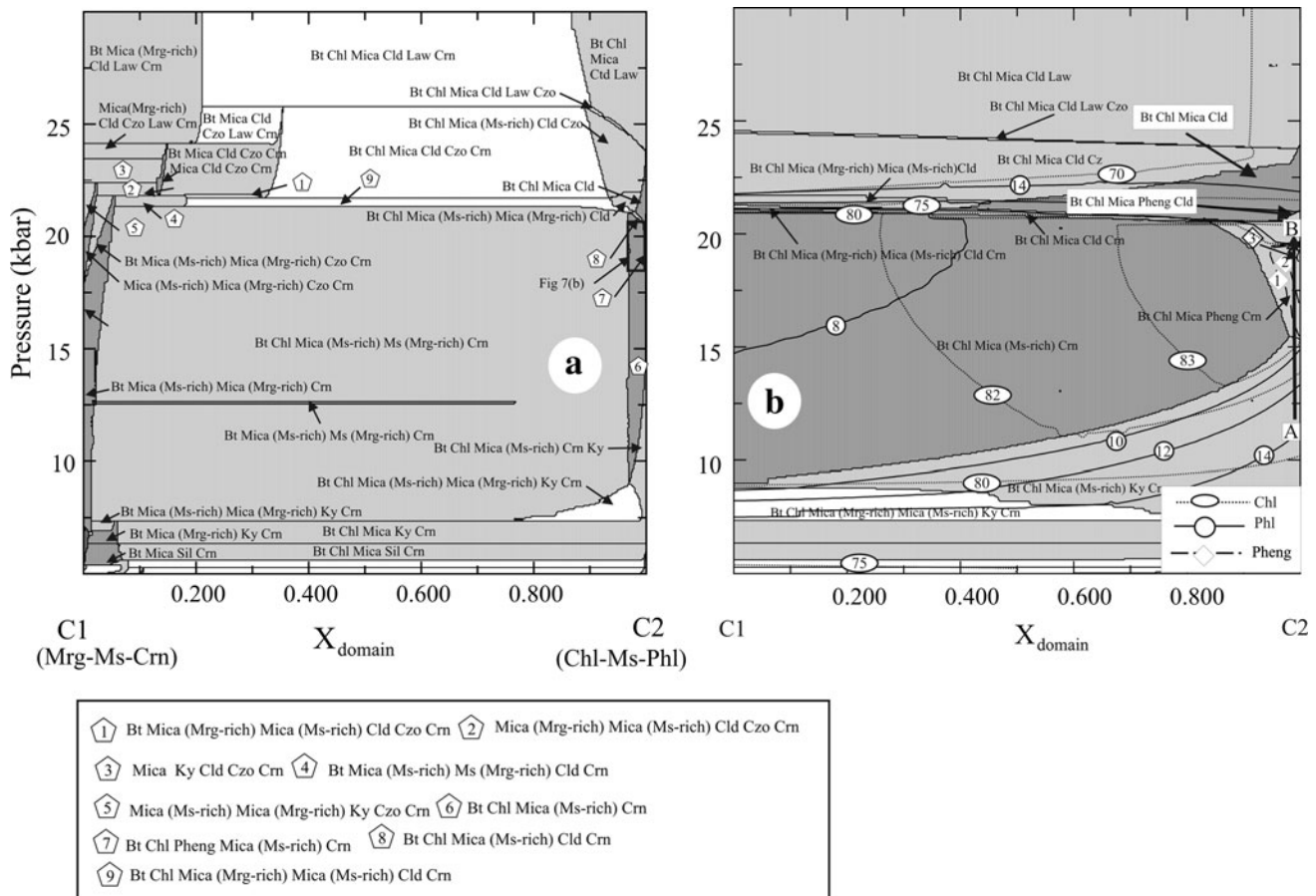
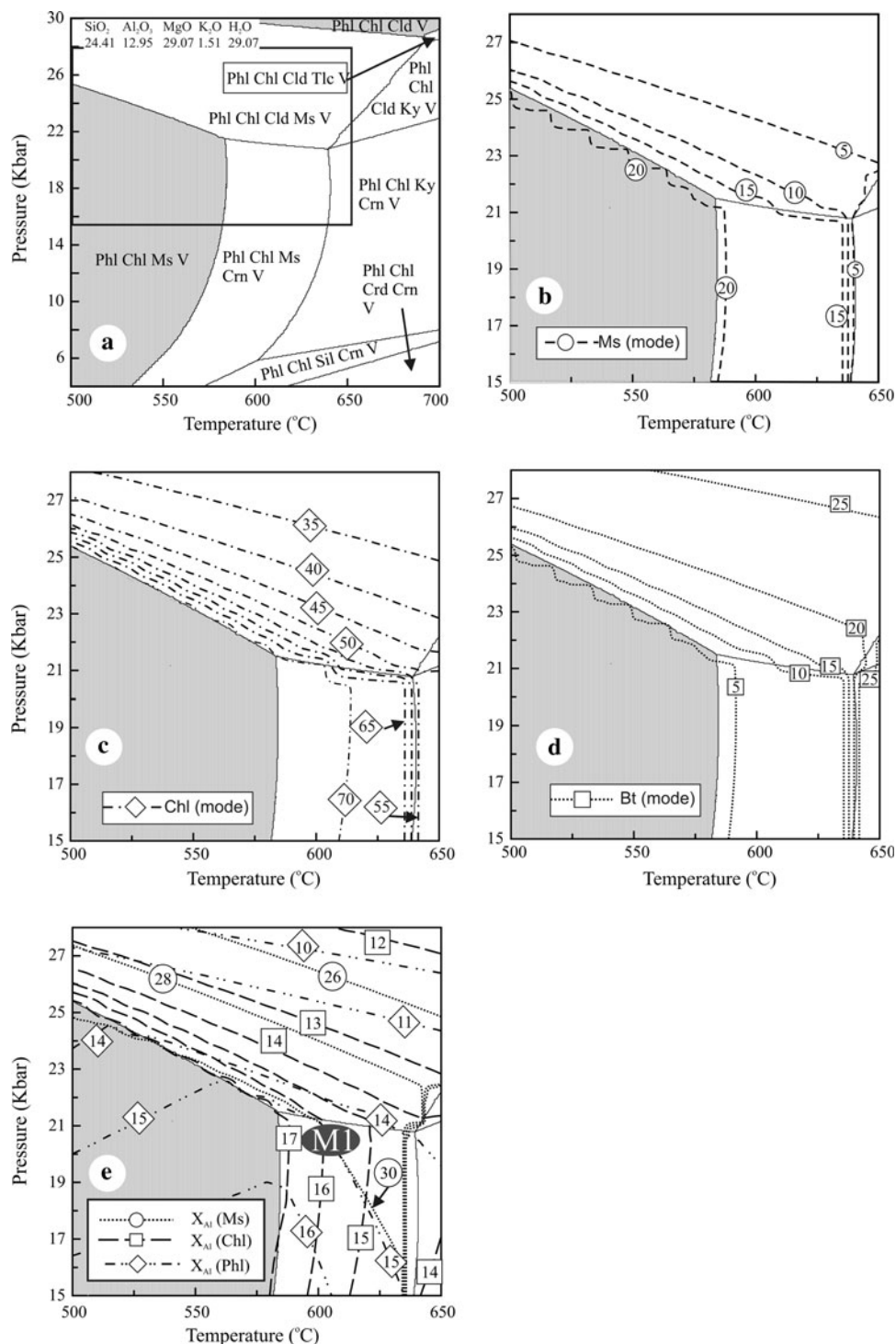


**Fig. 7** NCKMASH P–X<sub>domain</sub> pseudosections (a–b), where X (domain) represents compositions bracketed by micro-domain compositions of the interfaces between (i) margarite-muscovite inner corona and corundum (C1) and (ii) muscovite-chlorite outer corona at matrix phlogopite-chlorite bearing foliation (C2). The salient feature of this compositional vector is the decrease in Al<sub>2</sub>O<sub>3</sub>, CaO and

increase in MgO, K<sub>2</sub>O and SiO<sub>2</sub> from C1 to C2. C1 and C2 bulk compositions in terms of molar proportions of SiO<sub>2</sub>: Al<sub>2</sub>O<sub>3</sub>: MgO: CaO: Na<sub>2</sub>O: K<sub>2</sub>O are, respectively, 30.06 : 57.27 : 1.87 : 9.14 : 0.95 : 0.71 and 33.83 : 15.55 : 49.33 : 0.01 : 0.02 : 1.27. Modes of phlogopite, phengite, muscovite, margarite, corundum, and chlorite are shown. See text for detailed discussion

**Fig. 8** Phase topology (**a**, **b**), mineral modes (**b**, **c** and **d**), and compositions of muscovite, biotite and chlorite (**e**) computed using KMASH P-T pseudosection analysis (Connolly 2005) for the phengitic-muscovite + chlorite corona layer in WS-5 (Table 6). Note the P-T limits for phase topology in (**b**) are shown as box in (**a**). See text for the method used to compute the effective composition of the coronal layer. Note contours of mineral modes and compositions are shown for the P-T range 500–650°C and 4–30 kbar. M1 (*embedded in filled ellipse*) is the possible metamorphic P-T condition for the formation of the phengitic muscovite–chlorite outer coronal layer, consistent with the compositions of the coronal phases in Tables 1, 6



#### KMASH and NCKMASH P-T pseudosections

In corona-related studies (Johnson and Carlson 1990; Carlson and Johnson 1991; Ashworth and Birdi 1990), estimating the composition of the effective reaction volume for corona formation, as distinct from the bulk composition of the rock (Hensen 1987; Dunkley et al. 1999; Nasipuri

et al. 2009), is complicated because of two reasons. First, the proportion in which the reactant phases react is difficult to estimate, and second, the composition of the reactant solid solution phases is modified. Therefore, the modal mineralogy and the compositions of the product phases are the only source for estimating the composition of the reaction volume. In this study, the effective composition

for corona-forming reaction (1) was calculated by multiplying the compositions of the product phases (phengitic-muscovite and chlorite) to the area percentage of the product phases e.g., phengitic-muscovite and chlorite (Table 6) in the outer collar from multiple element images (Fig. 3). The area percentage of the phases was estimated using ImageJ software after tracing the outlines of the minerals. The area percentages of minerals in the intergrowth were difficult to estimate because of problem in distinguishing the two minerals in the fine-grained ( $<3\text{ }\mu\text{m}$ ) intergrowth, and the presence of corroded matrix phases (phlogopite and corundum). The problem was partially overcome by selecting domains in the outer collar in which the coronal phases are among the coarsest. In the next step, the coronal zone was divided into several sub-domains, but with considerable overlap (ca. 50%). Within each sub-domain, the estimated area percentages of chlorite and muscovite varied greatly. The average area percentage of chlorite and muscovite obtained from the different sub-domains was multiplied by the average compositions of the minerals to calculate the effective bulk composition for each sub-domain. The mean composition of these sub-domains was taken to correspond with the effective composition of the volume for reaction (1). The same approach was applied to compute the effective composition of the margarite-muscovite bi-phase corona (reaction 2).

In KMASH P-T pseudosection (Fig. 8a), the stability of phlogopite + corundum + muscovite + chlorite + vapor assemblage is restricted to temperatures between 525 and 625°C and pressures between 5 and 22 kbar. The modal proportion of phlogopite decreases and that of muscovite and chlorite increases toward the corundum-out curve from the phlogopite–chlorite–muscovite–corundum–vapor-bearing field (Fig. 8b–d). The variations support reaction

(1) (tie line intersection in Fig. 4a) that produced phengitic muscovite and chlorite symplectite at the expense of corundum and phlogopite. Figure 8e shows isopleths of  $X_{\text{Al}}$ , (Ms) and the modal proportion of  $\text{Al}_2\text{O}_3$  with respect

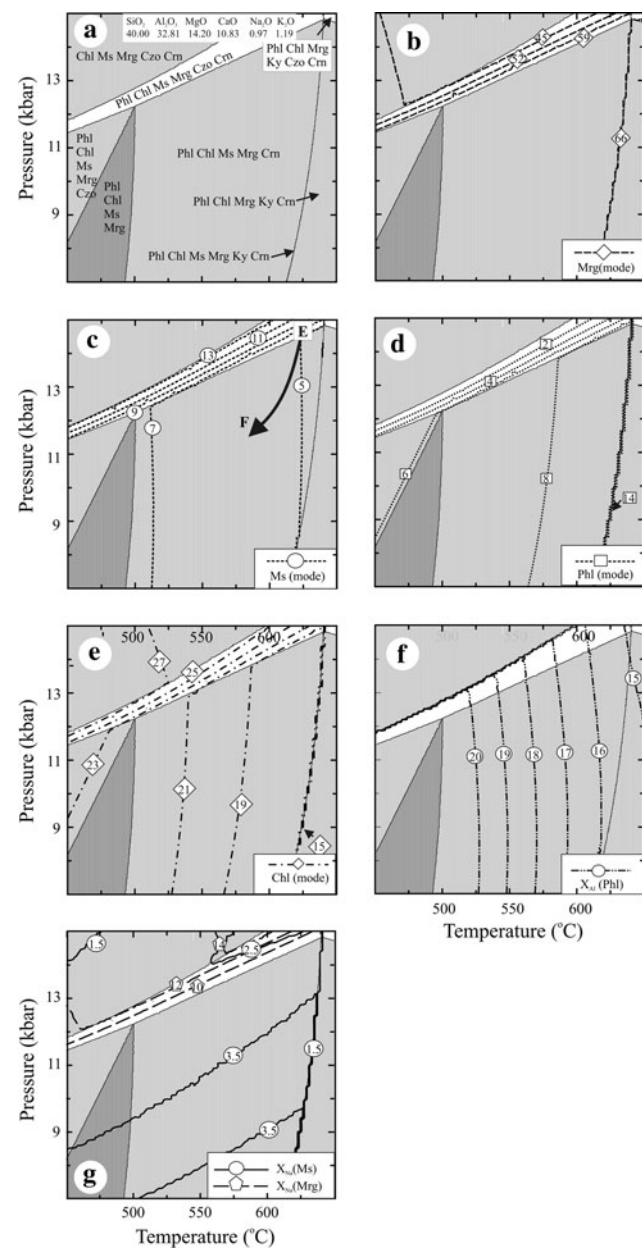


**Fig. 9** Phase topology (a, b), mineral modes (b–d) and compositions in terms of selected isopleths for chlorite (e), phlogopite (f) and muscovite, margarite (g) margarite, chlorite and muscovite computed using NCKMASH P-T pseudosection analysis (Connolly 2005) for the muscovite–margarite corona layer in WS-2. See text for the method used to compute effective composition of the coronal layer. Note contours of mineral modes and compositions are shown for the P-T range 450–650°C and 7–15 kbar. E → F is the possible decompression-cooling path for the rock, consistent with the theoretically determined isopleths and the measured compositions of minerals (Tables 1, 6)

**Table 6** Area % of product phases in coronal layers in Fig. 3

Area percentage of product phases in coronal layers					
Outer layer		Inner layer			
Ws5		Ws2			
Ms	Chl	Marg	Chl	Ms	
Box 1	16.21	83.79	Box 1	46.62	40.18
Box 2	21.52	78.48	Box 2	53.49	27.02
Box 3	20.83	79.17	Box 3	76.00	16.96
Box 4	16.11	83.89	Box 4	84.00	10.40
Box 5	6.75	93.25	Box 5	69.29	19.03
Box 6	31.95	68.05	Mean	0.66	0.23
Box 7	27.49	72.51			0.11
Box 8	53.72	46.28			
Box 9	75.39	24.61			
Mean	30.00	70.00			

to modal  $\text{SiO}_2$  and  $\text{MgO}$  from average mineral composition of muscovite, biotite, and chlorite. Average  $X$  (Al) in chlorite and muscovite from the outer layer is ca. 16% and ~30%, respectively based on microprobe analyses of 20 muscovite and 18 chlorite grains from the coronal domain in WS5. The average  $X_{\text{Al}}$  modal isopleths for the product phases, i.e., chlorite (ca. 16%) and muscovite (ca. 30%) intersect at about 600°C, 22 kbar. This P–T value is in broad agreement with the estimated P–T from convergent reactions (Fig. 6a) and P–X pseudosection (Fig. 7a).

The stabilization of margarite-muscovite corona is explained by the results of P–T pseudosection (NCKMASH) computations (Fig. 9a–g). In the high-pressure side, the clinzozoisite-out line from the field of phlogopite–chlorite–muscovite–margarite–clinzozoisite–corundum has a shallow positive slope indicating strong pressure dependence on the incoming of margarite (Fig. 9a). The modal isopleths of margarite (Fig. 9b) in the phlogopite–chlorite–muscovite–margarite–clinzozoisite–corundum field are almost parallel to the clinzozoisite and corundum-out reactions, showing an increase in its modal proportion with progressive consumption of clinzozoisite and corundum. The modal isopleths of muscovite, chlorite and phlogopite are parallel to each other in the phlogopite–chlorite–muscovite–margarite–clinzozoisite–corundum field but are disposed at a low angle to the clinzozoisite and corundum-out line. Formation of chlorite–muscovite–margarite at the expense of phlogopite–corundum–clinzozoisite is observed with decompression and cooling along path EF (Fig. 9a–e). The isopleths of mineral

compositions are shown in Fig. 9f, g. The modal  $X_{\text{Al}}$  isopleths for phlogopite (Fig. 9f) increases along the path EF, supporting our argument that the high eastonite component of relict phlogopite in the muscovite–chlorite symplectite reflects re-equilibration during decompression and cooling. Values of  $X_{\text{Na}}$  isopleths for margarite increase with pressure and is accompanied by decrease in  $X_{\text{Na}}$  of muscovite. Such a relation clearly indicates that the paragonite component of margarite was derived from muscovite.

In summary, thermo-barometry based on multi-reaction convergence (Fig. 6) and analyses of phase equilibria in P–X pseudosections (Fig. 7) and P–T pseudosections (Figs. 8, 9) indicate that the phengitic-muscovite + chlorite coronal layer around corundum porphyroblasts formed at 18–20 kbar, 620–640°C. Subsequently, the rock was decompressed to 10–12 kbar at near isothermal conditions that led to the stabilization of margarite + muscovite-bearing inner coronal layer.

### Timing of high-pressure metamorphism

The timing of the high-pressure metamorphism was constrained by dating monazite and zircon, the two common U–Th–Pb bearing accessory minerals in the rocks. Two distinct textural types of monazite can be identified. One group comprises euhedral grains with well-developed crystal faces, whereas the other has grains with strongly embayed and corroded boundaries (Figs. 2c, 10, 11). Both

**Fig. 10** BSE images of post-tectonic metamorphic monazite overgrowing the high-P micaceous foliation. Representative spot ages of analyzed grains are also given

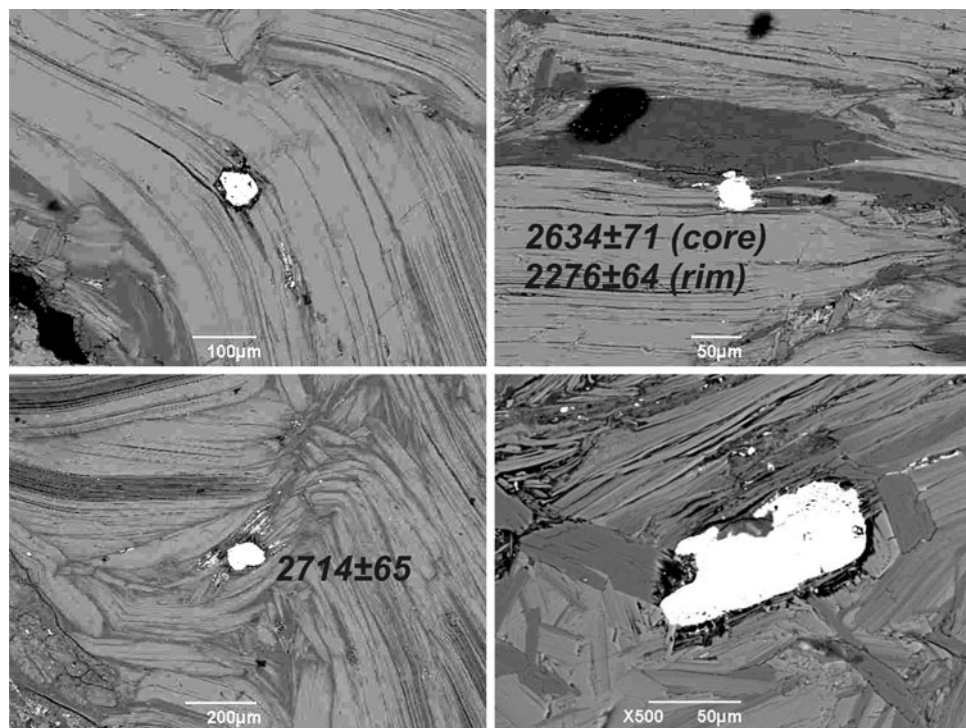
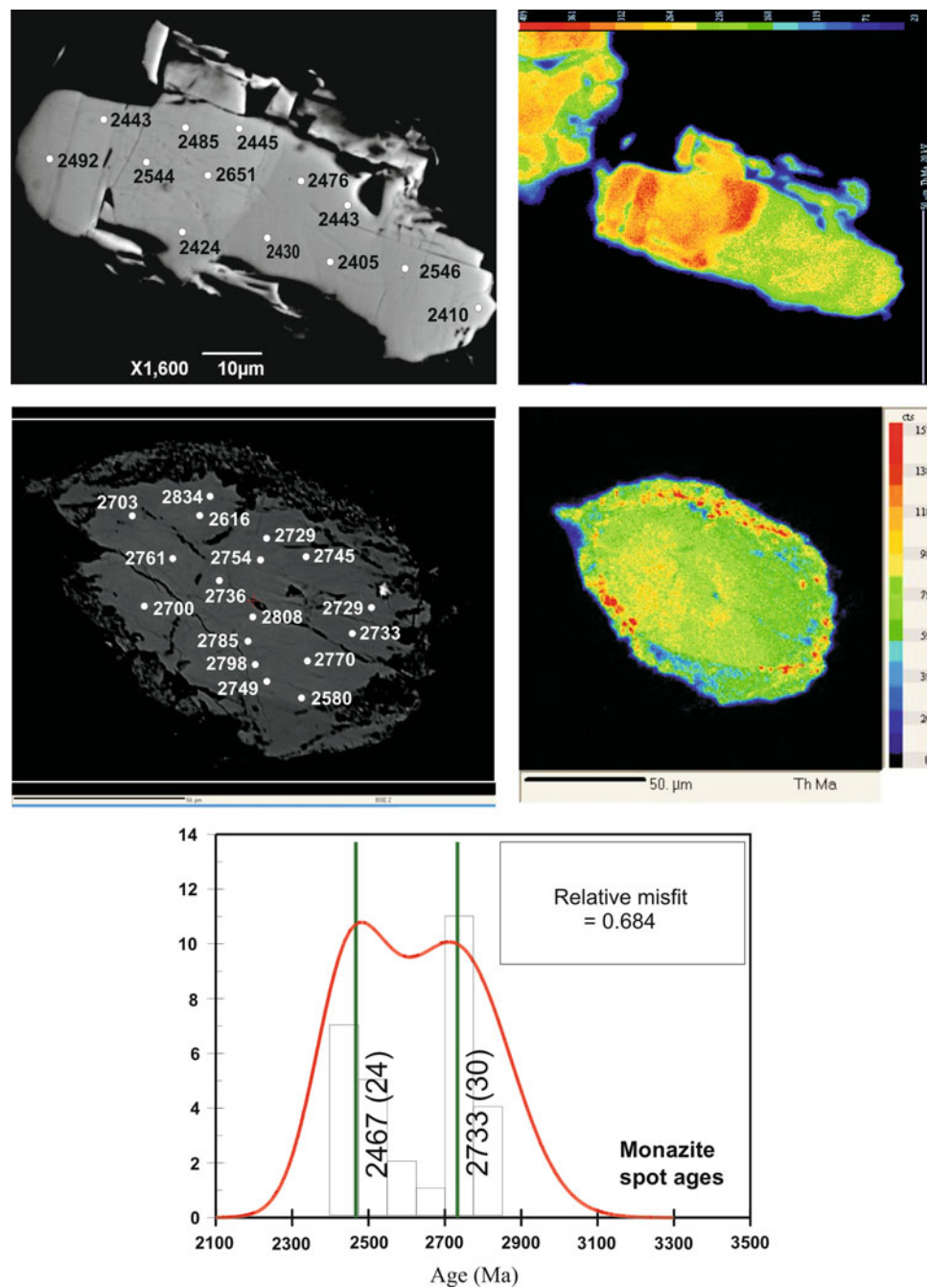


**Fig. 11** BSE (left panels) and Th X-ray maps (right panels) of the two textural types of monazite in the rocks. EPMA monazite spot ages are marked on the BSE images. The bottom panel *c* is an age probability density plot illustrating that the monazite ages can be unmixed into two Archean Gaussian age populations



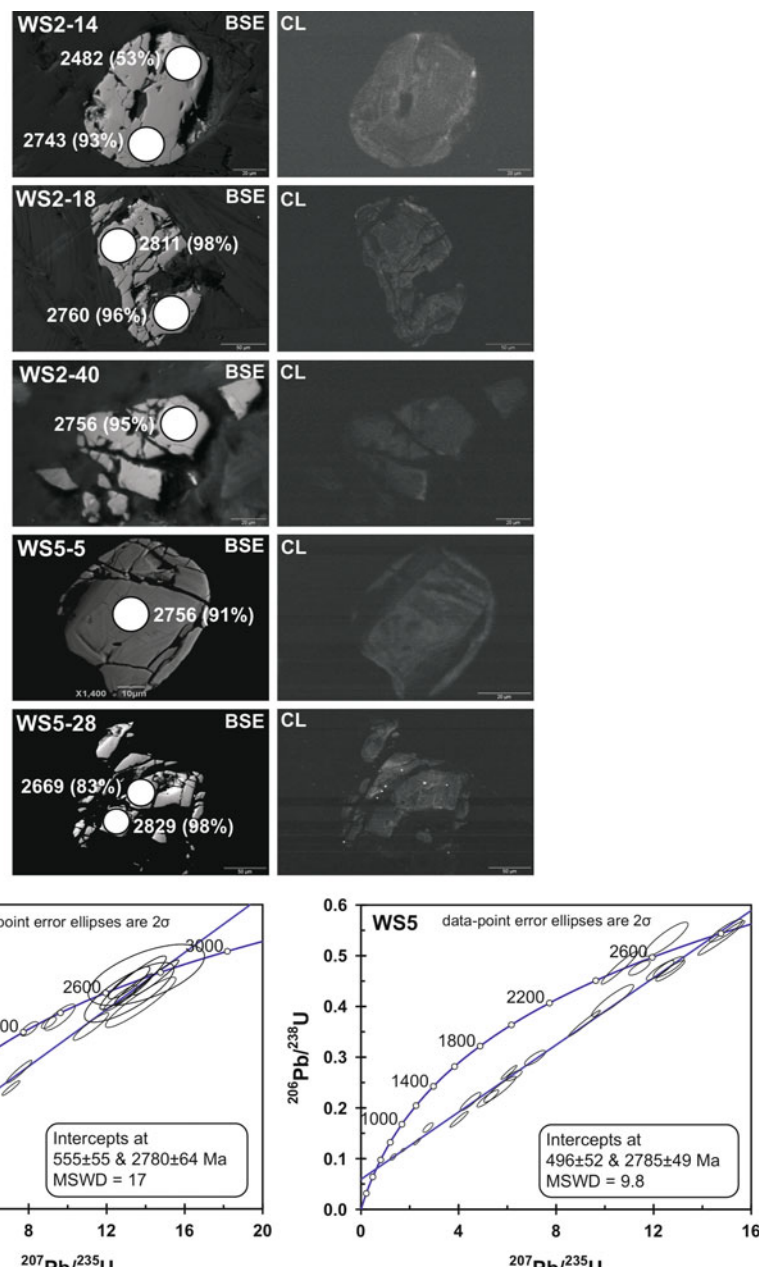
textural types overgrow the high-pressure micaceous foliation, clearly indicating that the monazites are of metamorphic origin and that the high-pressure metamorphism predates the growth of monazite in the rock (Fig. 10). The embayed grains give ages of  $2,737 \pm 127$  Ma ( $2\sigma$ ), while the euhedral grains lacking coronal alteration are  $2,476 \pm 139$  Myr ( $2\sigma$ ) old. The rim of one grain gives a younger age of  $2,276 \pm 64$  Ma (Table 7, electronic supplementary material, Fig. 11). Assuming the two dominant age groups, i.e., 2.74 Ga and 2.48 have Gaussian distribution and using the Sambridge and Compston (1994)

algorithm (Ludwig 2001), the monazite spot ages can be unmixed into two populations at  $2,733 \pm 30$  Ma (57%) and  $2,467 \pm 24$  Ma (43%) identical to the averages of spot ages from the two textural types of monazite in the rocks (Fig. 11). The Neoarchean ages obtained from these post-tectonic monazites indicate that the phlogopite + chlorite + corundum high-P assemblage is older than 2.73 Ga. The 2.47–2.28 Ga younger ages can be interpreted to be dating growth of new euhedral monazite grains possibly related to the decomposition of corundum during decompression.

U–Pb isotopic dating of zircons from two samples (WS2 and WS5) using laser ablation inductively coupled plasma mass spectrometry (LA-ICPMS) corroborates the results of monazite chemical dating that established a Neoarchean age for the high-pressure metamorphism (Table 8, electronic supplementary material). Back scatter electron (BSE) and cathodoluminescence (CL) images show that the zircon grains are fractured and lack any well-defined internal zonation (Fig. 12). Only a few of them preserve a diffuse relict zonation similar to that seen in re-equilibrated zircons. These internal structures indicate that the zircon grains re-equilibrated and recrystallized during metamorphism and hence record metamorphic or discordant ages.

**Fig. 12** BSE (left panel) and CL images (right panel) of selected zircon grains from samples WS2 and WS5 showing the laser ablation spots (sizes not to scale). The highly fractured zircon grains with diffuse or no internal zonation may have re-equilibrated and record metamorphic ages. Bottom panels are concordia plots of the U–Pb isotope data. Spot ages from zircon in the two samples define a discordia with upper and lower concordia intercept ages of ca. 2.78 and ca. 0.5 Ga

For zircons in sample WS2, the  $^{207}\text{Pb}/^{206}\text{Pb}$  spot ages range between 2,904 and 1,440 Ma and consist of concordant as well as discordant points. The concordant populations have ages of ca. 2.73 Ga, ca. 2.43 Ga, ca. 2.24 Ga, and ca. 1.58 Ga of which the 2.73 Ga, 2.43 Ga and 2.24 Ga ages are identical to those from post-tectonic metamorphic monazite overgrowing the high-pressure foliation in the rock. The discordant data points define a discordia with upper and lower concordia intercept ages of  $2,780 \pm 64$  and  $555 \pm 55$  Ma, respectively. For zircon grains in WS5, the  $^{207}\text{Pb}/^{206}\text{Pb}$  spot ages range from 2,829 to 1,476 Ma and again consist of both concordant and discordant data. The discordant analyses define a discordia upper and lower



intercept ages of  $2,785 \pm 49$  Ma and  $496 \pm 52$  Ma, identical to the dominant age populations in sample WS2 (Fig. 12). The upper intercept zircon ages from these two samples are also indistinguishable within uncertainty from the ages obtained from metamorphic monazite overgrowing the high-pressure micaceous foliation. Zircon grains that give concordant ages identical to the upper intercept ages from the two samples usually lack any internal zonation or show a relict and chaotic zoning, similar to that in recrystallized metamorphic zircon. These ca. 2.78 Ga zircon or zones therein represent domains that re-equilibrated during metamorphism. Because similar ages from metamorphic monazites clearly postdate the high-pressure mineral assemblage of the rock, it can be argued that the high-pressure metamorphism is at least 2.78 Gyr old. The lower discordia intercept can be interpreted as due to Pb loss during a late Neoproterozoic/early Paleozoic event.

## Tectonic implications

The oldest high-pressure metamorphic rocks reported so far in the Indian peninsula are of Mesoproterozoic age (1.7–1.5 Ga) e.g., ca. 12–15 kbar in the Aravalli-Delhi Mobile Belt (Saha et al. 2008), 10–12 kbar in the Singhbhum Mobile Belt (Mahato et al. 2008), and ca. 10 kbar in the Central Indian Tectonic Zone (Bhowmik et al. 2006). The >2.78 Ga age for high-P corona formation in schists from the Bundelkhand craton is possibly the oldest yet reported from the Indian Precambrian complexes. The ca. 2.78 Ga metamorphic zircons may have formed by pervasive re-equilibration of older zircons ( $3,270 \pm 3$  Ma; Mondal et al. 2002) from basement gneisses–greenstone in the Bundelkhand craton. The 2.48 Ga ages from euhedral monazite grains in the rock broadly coincide with the age of emplacement of expansive granitic suite of rocks in the Bundelkhand craton (2.55–2.49 Ga; Mondal et al. 2002; Jourdan et al. 2008). This event is not recorded in zircon and may be related to thermal metamorphism and growth of new monazite during this magmatic activity. The inferred high-P Archean metamorphism documented from the Bundelkhand craton in India adds to the growing body of evidence (Rapp et al. 2003; Moyen et al. 2006; Menneken et al. 2007) supporting the operation of modern day-like plate tectonic processes during the Archean.

**Acknowledgments** JKP thanks the Department of Science and Technology (DST) for providing financial support (grant # ESS/16/195/2003). DU and JB acknowledge K. Mezger (Munster) for providing opportunity to do LA-ICPMS analysis on zircons at short notice. V. Balaram of NGRI provided XRF analysis of bulk samples of the “white schists”. Electron probe microanalyses, element imaging (CAMECA SX-100), and back-scattered electron imaging (JEOL JSA 6490) of the samples were carried out in the DST (India)-

sponsored National EPMA Facility at the Department of Geology and Geophysics, Indian Institute of Technology, Kharagpur, India. The manuscript was reviewed by NM Kelly and an anonymous reviewer. Their thoughtful comments greatly helped in improving the scientific content and presentation.

## References

- Abbott RN, Greenwood JP (2001) Retrograde metamorphism of eclogite in the Southern Appalachian Mountains, U.S.A.; a case involving seamount subduction? *J Met Geol* 19:433–443
- Agard P, Goffe B, Touret-Jacques L-R, Vidal O (2000) Retrograde mineral and fluid evolution in high pressure metapelites (Schists Lustres Unit, Western Alps). *Contrib Mineral Petrol* 140:296–315
- Ashworth JR, Birdi JJ (1990) Diffusion modeling of coronas around olivine in an open system. *Geochim Cosmochim Acta* 54:2389–2401
- Ashworth JR, Shepley VS (1997) Diffusion modeling of metamorphic layered coronas with stability criterion and consideration of affinity. *Geochim Cosmochim Acta* 61:3671–3689
- Ashworth JR, Birdi JJ, Emmett TF (1992) Diffusion in coronas around clinopyroxene modeling with local equilibrium and steady state, and a non-steady modification to account for zoned actinolite-hornblende. *Contrib Mineral Petrol* 109:307–325
- Balashov VN, Lebedeva MI (1991) Macrokinetic model of origin and development of a monomineralic bimetasomatic zone. In: Perchuk LL (ed) *Progress in metamorphic and magmatic petrology*. Cambridge University Press, London, pp 167–195
- Basu AK (1986) Geology of parts of the Bundelkhand Granite Massif, Central India. *Rec Geol Surv India* 101:61–124
- Bhowmik SK, Basu Sarbadhikari A, Wilde S (2006) 1.6 Ga metamorphic re-heating and subsequent compression of UHT granulites from the Central Indian Tectonic Zone. In: M Brown, PM Piccoli (eds) *International conference with program and abstracts on the granulites and granulites*. Brasilia, Brazil, 16 pp
- Brown M (2007) Metamorphic conditions in orogenic belts: a record of secular change. *Int Geol Rev* 49:193–234
- Brown M (2009) Metamorphic patterns in orogenic systems and the geological record. In: Cawood PA, Krone A (eds) *Earth accretionary systems in space and time*, vol 318. The Geological Society, London, Special Publications, pp 37–74
- Carlson WD, Johnson CD (1991) Coronal reaction textures in garnet amphibolites of the Llano Uplift. *Am Mineral* 76:756–772
- Carswell DA, Wilson RN, Zhai M (2000) Metamorphic evolution, mineral chemistry and thermobarometry of schists and orthogneisses hosting ultra-high pressure eclogites in the Dabieshan of Central China. *Lithos* 52:121–155
- Chatterjee ND (1976) Margarite stability and compatibility relations in the system CaO–Al<sub>2</sub>O<sub>3</sub>–SiO<sub>2</sub>–H<sub>2</sub>O as a pressure–temperature indicator. *Am Mineral* 61:699–709
- Coggon R, Holland TJB (2002) Mixing properties of phengitic micas and revised garnet–phengite thermometers. *J Met Geol* 20:683–696
- Connolly JAD (2005) Computation of phase equilibria by linear programming: a tool for geodynamic modeling and its application to subduction zone decarbonation. *Earth Planet Sci Lett* 236:524–541
- Cuthbert SJ, Carswell DA (1990) Formation and exhumation of medium temperature eclogites in the Scandinavian Caledonides. In: Carswell DA (ed) *Eclogite facies rocks*. Blackie, Glasgow, pp 180–203

- Dunkley DJ, Clarke GL, Harley SL (1999) Diffusion metasomatism in silica-undersaturated sapphirine-bearing granulite from Rundoodle Peak, Framnes Mountains, east Antarctica. *Contrib Mineral Petrol* 134:264–276
- Ernst WG (1988) Subduction zone tectonics inferred from retrograde blueschist P-T-time paths. *Abstr Prog Geol Soc Am* 20:159
- Faryad SW, Hoinkes G (2006) Reaction textures in Al-rich metabasite; implication for metamorphic evolution of the eastern border of the Austroalpine basement units. *Lithos* 90:145–157
- Fisher GW, Elliott D (1974) Criteria for quasi-steady diffusion and local equilibrium in metamorphism. In: AW Hofmann et al (eds) *Geochemical transport and kinetics*. Carnegie Institution of Washington Publication, Washington, 634:231–241
- Fisher GW, Lasaga AC (1981) Irreversible thermodynamics in petrology. *Rev Mineral* 8:171–209
- Frank E (1983) Alpine metamorphism of calcareous rocks along a cross-section in the Central Alps: occurrence and breakdown of muscovite, margarite and paragonite. *Schw Min Pet Mitt* 63:37–93
- Gao J, Klemd R (2001) Primary fluids entrapped at blueschist to eclogite transition: evidence from the Tia Shan meta-subduction complex in north-eastern China. *Contrib Mineral Petrol* 142:1–14
- Gao J, Klemd R, Zhang L, Wang Z, Xiao X (1999) P-T path of high-pressure/low-temperature rocks and tectonic implications in the western Tia Shan Mountains, NW China. *J Met Geol* 17:621–636
- Gibson GM (1979) Margarite in kyanite- and corundum-bearing anorthosite, amphibolite, and hornblendite from Central Fiordland, New Zealand. *Contrib Mineral Petrol* 68:171–179
- Goswami JN, Mishra S, Wiedenbeck M, Ray SL, Saha AK (1995) 3.55 Ga old zircon from Singhbhum-Orissa Iron Ore Craton, eastern India. *Curr Sci* 69:1008–1012
- Hensen BJ (1987) P-T grids for silica-undersaturated granulites in the systems MAS ( $n + 4$ ) and FMAS ( $n + 3$ )—tools for the derivation of P-T paths of metamorphism. *J Met Geol* 5:255–271
- Holland TJB, Powell R (1998) An internally-consistent thermodynamic dataset for phases of petrological interest. *J Met Geol* 16:309–344
- Holland TJB, Baker J, Powell R (1998) Mixing properties and activity-composition relationships of chlorites in the system MgO–FeO–Al<sub>2</sub>O<sub>3</sub>–SiO<sub>2</sub>–H<sub>2</sub>O. *Eur J Mineral* 10:395–406
- Johnson CD, Carlson WD (1990) The origin of olivine-plagioclase coronas in metagabbros from the Adirondack Mountains, New York. *J Met Geol* 8:697–717
- Jourdan F, Reimold WU, Armstrong RA, Pati JK, Renne P, Koeberl C (2008) Elusive age of the Paleoproterozoic Dhala impact structure, India: first SHRIMP U-Pb and argon chronological results. 39th Lunar Planet Science Conference CD-ROM, Abstract: 1244
- Komiya T, Maruyama S, Hirata T, Yurimoto H (2002) Petrology and geochemistry of MORB and OIB in the mid-Archean North Pole region, Pilbara craton, Western Australia: implications for the composition and temperature of the upper mantle at 3.5 Ga. *Int Geol Rev* 44:988–1016
- Kretz R (1983) Symbols of rock forming minerals. *Am Mineral* 68:277–279
- Lichtner PC (1988) The quasi-stationary state approximation to coupled mass transport and fluid-rock interaction in a porous medium. *Geochim Cosmochim Acta* 52:143–165
- Ludwig KR (2001) User's manual for Isoplot/ex rev. 2.49: a geochronological toolkit for Microsoft Excel. Berkeley Geochron Center Spec Publ 1a:1–56
- Mahato S, Goon S, Bhattacharya A, Mishra B, Bernhardt H-J (2008) Thermo-tectonic evolution of the North Singhbhum Mobile Belt (Eastern India): a view from the western part of the belt. *Precamb Res* 162:70–85
- Malviya VP, Arima M, Pati JK, Kaneko Y (2006) Petrology and geochemistry of metamorphosed basaltic pillow lava and basaltic komatiite in Mauranipur area: subduction related volcanism in Archean Bundelkhand craton, Central India. *J Mineral Petrol Sci Jpn* 101:199–217
- Menneken M, Nemchin AA, Geisler T, Pidgeon RT, Wilde SA (2007) Hadean diamonds in zircon from Jack Hills, Western Australia. *Nature* 448:917–920
- Millonig L, Zeh A, Gerdes A, Klemd R (2008) Neoarchaean high-grade metamorphism in the Central Zone of the Limpopo Belt (South Africa): combined petrological and geochronological evidence from the Bulai pluton. *Lithos* 103:333–351
- Mishra S, Deomurari MP, Wiedenbeck M, Goswami JN, Ray S, Saha AK (1999) <sup>207</sup>Pb/<sup>206</sup>Pb zircon ages and the evolution of the Singhbhum Craton, eastern India: an ion microprobe study. *Precamb Res* 93:139–151
- Mondal MEA, Ahmad T (2001) Bundelkhand mafic dykes, Central Indian shield: implication for the role of sediment subduction in Proterozoic crustal evolution. *Island Arc* 10:51–67
- Mondal MEA, Goswami JN, Deomurari MP, Sharma KK (2002) Ion microprobe <sup>207</sup>Pb/<sup>206</sup>Pb ages zircons from Bundelkhand massif, north India: implications for crustal evolution of the Bundelkhand-Aravalli protocontinent. *Precamb Res* 117:85–100
- Moyen JF, Stevens G, Kisters A (2006) Record of mid-Archean subduction from metamorphism in Barberton Terrain, South Africa. *Nature* 442:559–562
- Nasipuri P, Bhattacharya A, Das S (2009) Metamorphic reactions in dry and aluminous granulites: a Perple\_X P-T pseudosection analysis of the influence of effective reaction volume. *Contrib Mineral Petrol* 157:301–311
- O'Brien PJ, Carswell DA (1993) Tectonometamorphic evolution of the Bohemian Massif: evidence from high pressure metamorphic rocks. *Geol Rundsch* 82:531–555
- Pati JK (1998) Specialized thematic studies of quartz reefs and mylonite zones in parts of Bundelkhand Granitoid Complex, southern U.P. *Geol Surv India Rec* 130:88–89
- Pati JK (1999) Study of granitoid mylonites and reef/vein quartz in parts of Bundelkhand Granitoid Complex (BGC). *Geol Surv India Rec* 131:95–96
- Pati JK, Patel SC, Pruseth KL, Malviya VP, Arima M, Raju S, Pati P, Prakash K (2007) Geology and geochemistry of giant quartz veins from the Bundelkhand craton, Central India and their implications. *J Earth Sys Sci* 116:497–510
- Pati JK, Reimold WU, Koeberl C, Pati P (2008a) The Dhala structure, Bundelkhand Craton, Central India—eroded remnant of a large Paleoproterozoic impact structure. *Meteorit Planet Sci* 43:1383–1398
- Pati JK, Raju S, Malviya VP, Bhushan R, Prakash K, Patel SC (2008b) Mafic Dykes of Bundelkhand Craton, Central India. Field, petrological and geochemical characteristics. In: Srivastava R et al (eds) *Indian dykes: geochemistry, geophysics and geochronology*. Narosa Publishing House, New Delhi, pp 547–569
- Powell R, Holland TJB (1999) Relating formulations of the thermodynamics of mineral solid solutions; activity modeling of pyroxenes, amphiboles, and micas. *Am Mineral* 84(1–2):1–14
- Rahaman A, Zainuddin SM (1993) Bundelkhand granite: an example of collision-related Precambrian magmatism and its relevance to the evolution of the Central Indian Shield. *J Geol* 101:413–419
- Rao MJ, Rao PGVS, Widdowson M, Kelley SP (2005) Evolution of Proterozoic mafic dyke swarms of Bundelkhand craton, Central India. *Curr Sci* 88:502–506
- Rapp RP, Shimizu N, Norman MD (2003) Growth of early continental crust by partial melting of eclogite. *Nature* 425:605–609

- Rubie DC (1990) Role of kinetics in the formation and preservation of eclogites. In: Carswell DA (ed) Eclogite facies rocks I. Blackie, Glasgow, pp 111–140
- Saha L, Bhowmik SK, Fukuoka M, Dasgupta S (2008) Contrasting episodes of regional granulite-facies metamorphism in enclaves and host gneisses from the Aravalli-Delhi Mobile Belt, NW India. *J Petrol* 49:107–128
- Sambridge MS, Compston W (1994) Mixture modeling of multi-component data sets with application to ion-probe zircon ages. *Earth Planet Sci Lett* 128:373–390
- Sarkar A, Bhalla JK, Bishui PK, Gupta SN, Singhai RK, Upadhyaya TP (1994) Tectonic discrimination of granitic rocks: studies on the early Proterozoic Bundelkhand Complex, Central India. *Ind Mineral* 45:103–112
- Sarkar A, Paul DK, Potts PJ (1996) Geochronology and geochemistry of mid-Archaean trondhjemite gneiss from the Bundelkhand Craton, Central India. *Rec Res Geol* 16:76–92
- Schliestedt M (1986) Eclogite–blueschist relationships as evidenced by mineral equilibria in the high pressure metabasic rocks of Sifnos (Cycladic Islands), Greece. *J Petrol* 27:1437–1459
- Sentiappan M (1976) Geology of the area along the Raksa Shear zone, Jhansi district, Uttar Pradesh. Symposium on the Archaean of the Central India, GSI, Nagpur, Nov 30–Dec 1. (Abstract)
- Sentiappan M (1981) Geology of the area along the Raksa Shear zone, Jhansi district, Uttar Pradesh. *Geol Surv India Spl Pub* 3:73–76
- Singh SP, Dwivedi SB (2009) Garnet–sillimanite–cordierite–quartz bearing assemblages from early Archean supracrustal rocks of Bundelkhand Massif, Central India. *Curr Sci* 97:103–107
- Singh SP, Singh MM, Srivastava P, Basu AK (2007) Crustal evolution in Bundelkhand area, Central India. *Him Geol* 28:79–101
- Spalla MI, Carminati E, Ceriani S, Oliva A, Battaglia D (1999) Influence of deformation partitioning and metamorphic re-equilibration on a P–T path reconstruction in the pre-Alpine basement of central Southern Alps (Northern Italy). *J Met Geol* 17:319–336
- Thompson JB Jr, Waldbaum DR (1969) Mixing properties of sanidine crystalline solutions. III. Calculations based on two-phase data. *Am Mineral* 54:811–838
- Vidal O, Parra T (2000) Exhumation paths of high pressure metapelites obtained from local equilibria for chlorite–phengite assemblages. *Geol Mag* 35:139–161
- Wallis S, Aoya M (2000) A re-evaluation of eclogite facies metamorphism in SW Japan: proposal for an eclogite nappe. *J Met Geol* 18:653–664
- White RW, Powell R, Clarke GL (2002) The interpretations of reaction textures in Fe-rich metapelitic granulite of Musgrave Block, Central Australia: constraints from mineral equilibria calculations in the system  $K_2O$ – $FeO$ – $MgO$ – $Al_2O_3$ – $SiO_2$ – $H_2O$ – $TiO_2$ – $Fe_2O_3$ . *J Met Geol* 20:41–55
- Wiedenbeck M, Alla P, Corfu F, Griffin WL, Meier M, Oberli F, von Quadt A, Roddick JC, Spiegel W (1995) Three natural zircon standards for U–Th–Pb, Lu–Hf, trace elements and REE analyses. *Geostand Geoanalytic Res* 19:1–23